Energy Conversion and Management 265 (2022) 115769

Contents lists available at ScienceDirect

Energy Conversion and Management

journal homepage: www.elsevier.com/locate/enconman

Characterization of wake interference between two tandem offshore floating vertical-axis wind turbines: Effect of platform pitch motion

Limin Kuang [a], Qi Lu [b], Xuan Huang [b], Leijian Song [b], Yaoran Chen [a], Jie Su [a], Zhaolong Han [a,c,d,e,*], Dai Zhou [a,c,d], Yongsheng Zhao [a], Yuwang Xu [a], Yijie Liu [f]

[a] State Key Laboratory of Ocean Engineering, School of Naval Architecture, Ocean and Civil Engineering, Shanghai Jiao Tong University, Shanghai 200240, China
[b] Shanghai Electric Wind Power Group Co., Ltd., Shanghai 200233, China
[c] Shanghai Key Laboratory for Digital Maintenance of Buildings and Infrastructure, Shanghai Jiao Tong University, Shanghai 200240, China
[d] Key Laboratory of Hydrodynamics of Ministry of Education, Shanghai Jiao Tong University, Shanghai 200240, China
[e] Institute of Polar and Ocean Technology, Institute of Marine Equipment, Shanghai Jiao Tong University, Shanghai 200240, China
[f] Department of Mechanical Engineering, The University of Tokyo, Tokyo 113-8654, Japan

ARTICLE INFO

Keywords:
Offshore floating VAWT
Wake interference
Platform pitch motion
Power performance
IDDES

ABSTRACT

The wake interference within the offshore wind farms, especially with the tandem arrangement scenario, affects the designed total power output. Also, the six degrees of freedom motions of the platforms not only can change the aerodynamics of the offshore floating wind turbines, but also may influence the wake interference between them. In the present study, the effect of the platform pitch motion on the wake interference between two tandem offshore floating vertical-axis wind turbines (VAWTs) is characterized using the improved delayed detached-eddy simulation (IDDES). First, the power performance of the downstream turbine (VAWT II) at different separation distances, $2D \le L_S \le 10D$, and tip speed ratios, $0.4 \le \mathrm{TSR}^{\mathrm{II}} \le 1.5$, are analyzed, assuming that the upstream turbine (VAWT I) is bottom-fixed and operates at an optimal $\mathrm{TSR}^{\mathrm{I}}$ of 1.2. Then, the effects of the pitch amplitude, $5^\circ \le A_P{}^{\mathrm{I}} \le 15^\circ$, and pitch period, $2T^{\mathrm{I}} \le T_P{}^{\mathrm{I}} \le 8T^{\mathrm{I}}$, on the wake interference are characterized by assuming that the platform pitch motion of VAWT I follows a prescribed simple harmonic law. The results show that locating VAWT II in the medium wake region of VAWT I, e.g., $L_S = 6D$, can appropriately balance the power performance and space cost of the bottom-fixed turbine array. Also, the platform pitch motion can reduce the mean velocity deficit in the core wake region of VAWT I. The mean wake deficit reduction increases the averaged power coefficient of VAWT II, e.g., up to 22.67% when $L_S = 6D$, $\mathrm{TSR}^{\mathrm{II}} = 1.2$, $A_P{}^{\mathrm{I}} = 15^\circ$, and $T_P{}^{\mathrm{I}} = 4T^{\mathrm{I}}$. In addition, relatively larger pitch amplitudes and smaller pitch periods will further alleviate the negative effect of the wake interference. This study may serve as a reference for designing offshore floating wind farms.

1. Introduction

The increasing concerns about climate change and environmental pollution have made the exploitation of clean energy an important issue worldwide [1,2]. Wind energy is a highly attractive option due to the abundant wind resources in the vast ocean [3]. The offshore wind turbines play a crucial role in harvesting the ocean wind energy, which can be classified into two categories based on the rotation axis direction, i.e., horizontal-axis wind turbines (HAWTs) and vertical-axis wind turbines (VAWTs) [4]. The HAWTs have been remarkably developed in the past few decades, and now they dominate the global commercial market [5]. Nevertheless, the VAWTs have the potential to catch up with the forerunners because of their unique advantages, including omnidirectionality, design simplicity, and low installation and maintenance costs [6,7].

The scalability and high space efficiency make the VAWTs a promising option for building wind farms [3,6]. However, the strong wake interference between the wind turbines may negatively affect the aerodynamics of the downstream wind turbines, thereby reducing the total power output of the wind farms [8]. In Horns Rev offshore wind farm, for example, the power output of the second row of the wind turbines can only reach 60% of the power output of the first row under

* Corresponding author at: State Key Laboratory of Ocean Engineering, School of Naval Architecture, Ocean and Civil Engineering, Shanghai Jiao Tong University, Shanghai 200240, China.
E-mail address: han.arkey@sjtu.edu.cn (Z. Han).

https://doi.org/10.1016/j.enconman.2022.115769
Received 2 February 2022; Received in revised form 13 April 2022; Accepted 14 May 2022
Available online 26 May 2022

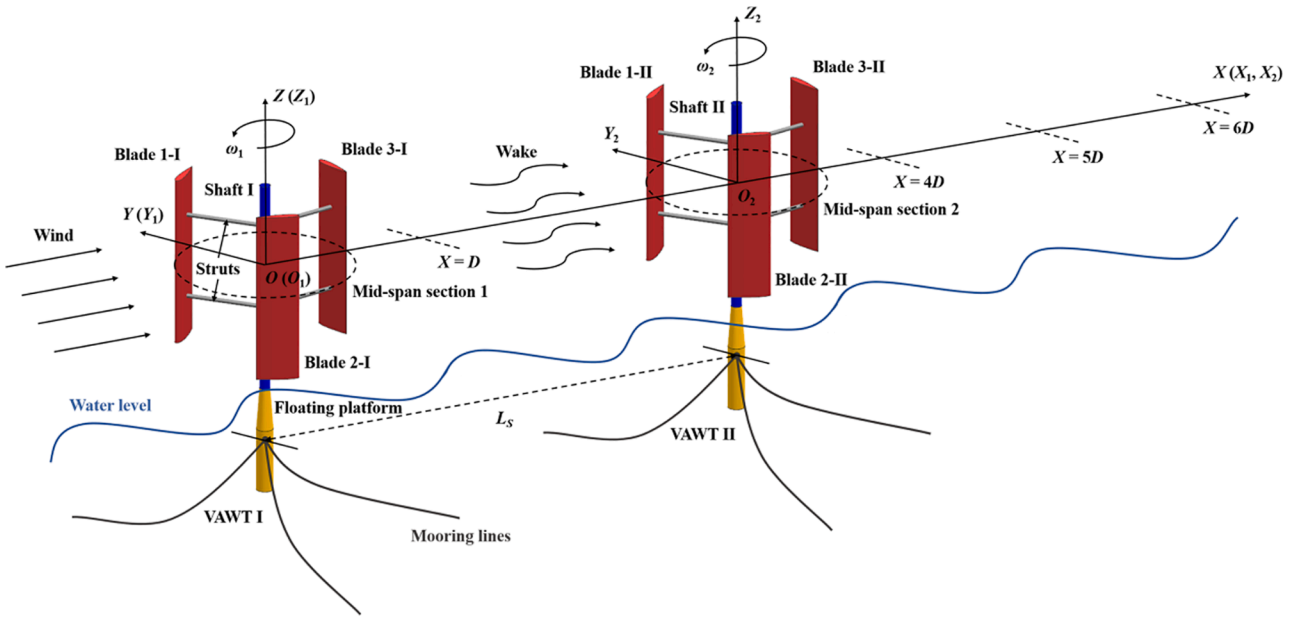

Fig. 1. Schematic of the two tandem offshore floating VAWTs. (Not to scale, floating platform and mooring lines are for illustration and are not considered in the simulations).

Table 1
Geometric features of the selected VAWT.

Feature	Symbol	Value
Airfoil	–	NACA0018
Blade number	*n*	3
Span length	*H*	0.800 m
Chord length	*c*	0.200 m
Rotor diameter	*D*	0.800 m
Shaft diameter	*d*	0.050 m

specific wind directions. Note that the power output can be lower in compact wind farms [9,10]. Therefore, investigating the wake interference within the turbine array is of great importance in the layout design of offshore wind farms. The wake of isolated wind turbines was extensively studied experimentally and numerically. Tescione et al. [11] employed particle image velocimetry (PIV) to investigate the flow structures in the near wake region of a typical VAWT. They analyzed the wake velocity distribution and the evolution of the blade tip vortices. Li et al. [12] conducted a series of field tests and measured the wake velocity of a two-straight-bladed VAWT. The results showed that the wake recovery of the VAWT was asymmetric, and the peak wake deficit decreased with the increase of the inflow velocity. Rolin et al. [13] used PIV and explored the wake characteristics of a small-scale VAWT immersed in the boundary layer flow. They found that two counter-rotating vortex pairs were formed in the downstream region of the VAWT, which would result in the cross-wind motion and reintroduce the streamwise momentum into the turbine wake.

The computational fluid dynamics (CFD) method is widely adopted for numerical simulations because of its capability to obtain critical flow information, e.g., wake pattern and vortical structures [14]. Abkar et al. [15] explored the wake structures of a three-straight-bladed VAWT using the large-eddy simulation (LES). They observed that the wake profile of the VAWT was self-similar and followed a Gaussian-like

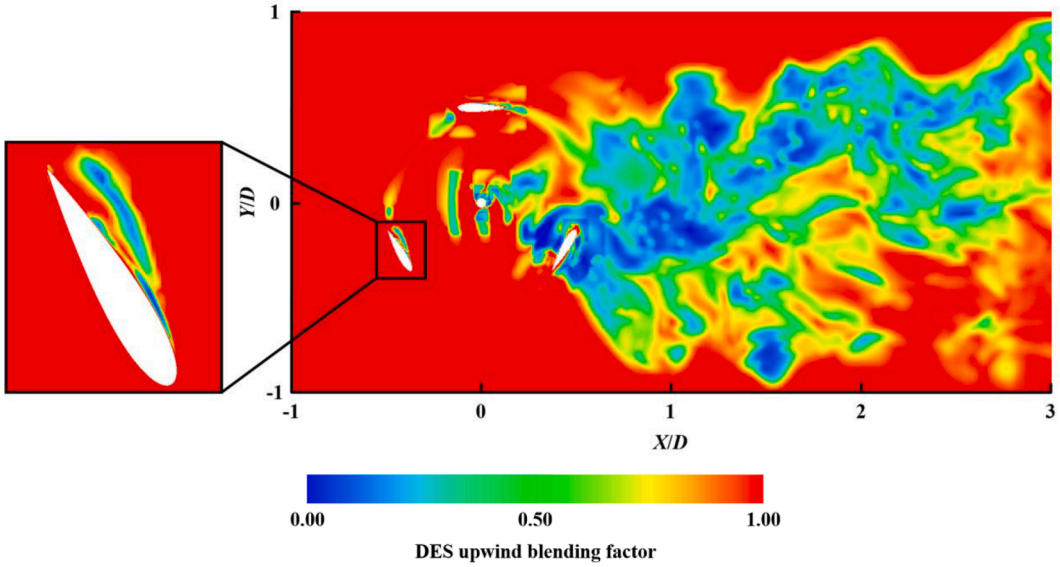

Fig. 2. Snapshot of the instantaneous flow pattern around the selected VAWT in the *X*-*Y* plane.

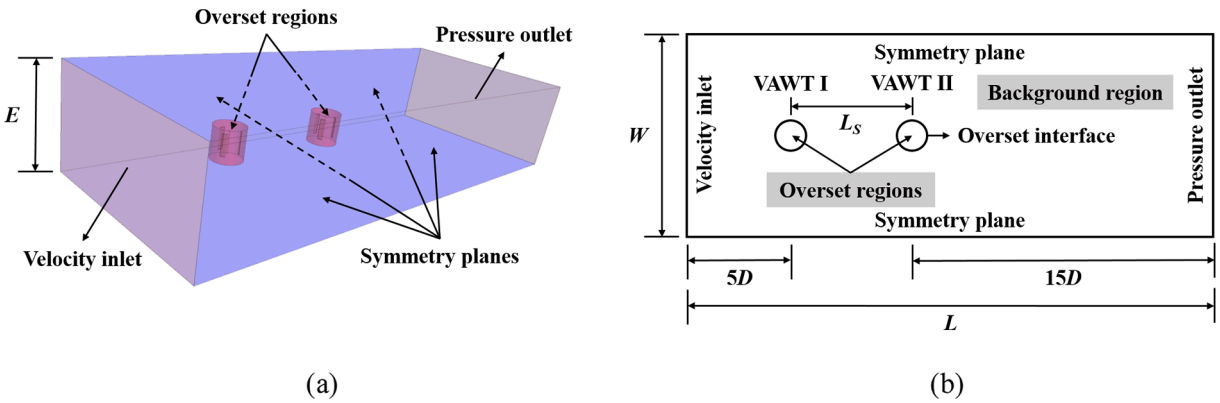

Fig. 3. Schematic of the computational domain: (a) overall view; (b) plan layout (not to scale).

distribution. Rezaeiha et al. [6] employed the unsteady Reynolds-Averaged Navier-Stokes (URANS) method to characterize the impact of the turbulence intensity (TI) on the near wake of a two-straight-bladed VAWT. The results showed that a higher TI could suppress the expansion of the turbine wake and reduce the velocity deficit. Posa [16] evaluated the influence of the tip speed ratio (TSR) on the wake development of a scaled VAWT using the LES. It was found that the turbine wake was highly dependent on TSR, in which the increased TSR would enlarge the momentum deficit and promote the wake recovery. In addition to the operational parameters, the correlation between the wake characteristics and the turbine geometry (e.g., solidity [17] and aspect ratio [18]) has also been extensively examined.

As numerous studies shed light on the wake of the isolated VAWTs and laid a solid foundation, the investigation of the wake interference within the turbine array reaches a fairly comprehensive level. Similar to HAWTs, some researchers focused on the mutual interaction between VAWTs in the conventional layout, e.g., tandem arrangement with a moderate to large separation distance. Zuo et al. [19] investigated the wake effect acting on a downstream VAWT located at 5 – 17 times the rotor diameter from the upstream one using the two-dimensional CFD simulations. The results showed that the power performance of the downstream VAWT improved linearly as the separation distance increased, and the wake effect could be neglected when this distance reached 15 times the rotor diameter. Kuang et al. [20] confirmed these results using the three-dimensional improved delayed detached-eddy simulation (IDDES) and further indicated that a higher TI could reduce the wake interference within the turbine array. Also, inspired by the pioneering studies of Dabiri [21] and Kinzel et al. [22], the potential performance improvement obtained from utilizing the blockage effect induced by the wake interference between the closely spaced VAWTs has received much attention. Zanforlin et al. [23] numerically analyzed the wake patterns of two VAWTs in a series of compact arrangements. They found that the key reasons for the corresponding performance improvement are the lateral flow velocity variation, wake contraction, and wind acceleration. On this basis, Sahebzadeh et al. [24] performed extensive CFD simulations to identify the optimal layout of two single-straight-bladed VAWTs. Some typical operational and geometric parameters of the VAWTs, e.g., wind direction [25], rotational direction [26], solidity [27], and blade pitch angle [28], were also included for further optimization. Besides, the wind tunnel tests conducted by Ahmadi-Baloutaki et al. [29], Lam et al. [30], and Su et al. [31] verified the influence of the array configuration on the wake interference and provided several useful suggestions for the layout design.

The offshore wind farms are gradually moving to the deep waters to further exploit the untapped ocean wind energy [32,33]. The offshore floating wind turbines, which are suitable for areas with a water depth greater than 50 m, have broad application prospects [32]. The six degrees of freedom motions of the platforms are one of the iconic features of floating wind turbines and are proven to have a great impact on the aerodynamics of the isolated ones [34,35]. It is therefore fascinating to see how these motion characteristics can influence the design of offshore wind farms with multiple floating rotors. However, the literature reveals that at the present state of the art, the bottom-fixed VAWTs are the main research objects. In contrast, the wake of the isolated floating VAWTs and the wake interference within the floating turbine array has been less focused on. Lei et al. [36] applied the SST k-ω IDDES to investigate the wake characteristics of a scaled offshore floating VAWT. They found that the platform pitch motion would significantly alter the wake pattern of the VAWT, thereby creating challenges for the analytical modeling of the turbine wake. To the best of the authors' knowledge, there have been no studies regarding the wake interference between the offshore floating VAWTs. Thus, this physical phenomenon is still unclear. Specifically, the inflow to the downstream turbine has multiple sources of unsteadiness, including the relative motion of the rotors and the dynamic wake of the oscillating upstream turbine [37]. This feature is expected to make the layout design principle of the floating turbine array different from that of the bottom-fixed one. Note that a few relevant experiments and numerical simulations were performed on HAWTs to support the design of the offshore floating wind farms [37,38,39]. Therefore, it is necessary to conduct the same research on VAWTs.

Given the above research gap, the present study aims to provide fundamental insight into the wake interference between the offshore floating VAWTs. The objective is to characterize the effect of the platform pitch motion on the power performance and flow structures of the turbine array. As one of the most basic and representative layouts, the scenario of two VAWTs in the tandem arrangement will be numerically analyzed. The upstream turbine is under the platform pitch motion and the downstream turbine is set to bottom-fixed. Note that the case in which both VAWTs are set to bottom-fixed will also be included for comparison. However, since the pitch characteristics of the downstream turbine are complicated to be determined, the case in which both VAWTs are under the platform pitch motion is not included. The main objectives of the present study are as follows:

- Exploring the basic layout pattern of the bottom-fixed turbine array. For this purpose, the power performance of the downstream turbine at different separation distances and the wake profile of the upstream turbine will be analyzed to provide a balanced solution for arranging the tandem bottom-fixed VAWTs.
- Elucidating the wake interference within the floating turbine array under the platform pitch motion. Thus, the power performance and aerodynamic load of the downstream turbine experiencing the wake interference from the pitching upstream turbine will be quantified. Also, a systematic comparison of the turbine aerodynamics will be conducted for the bottom-fixed and pitching cases. The flow

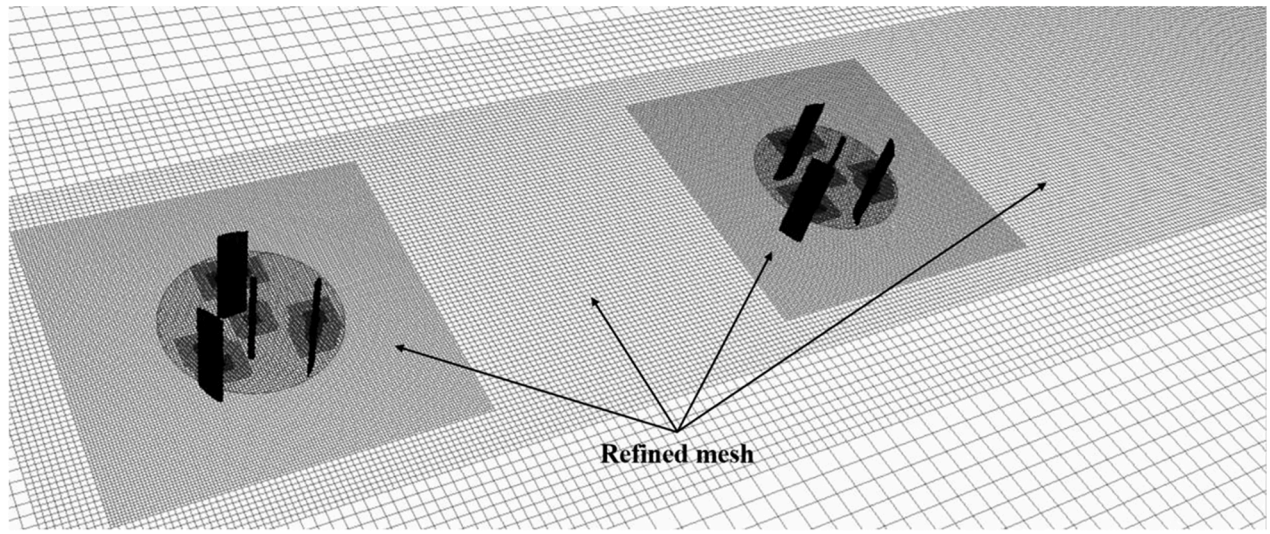

(a)

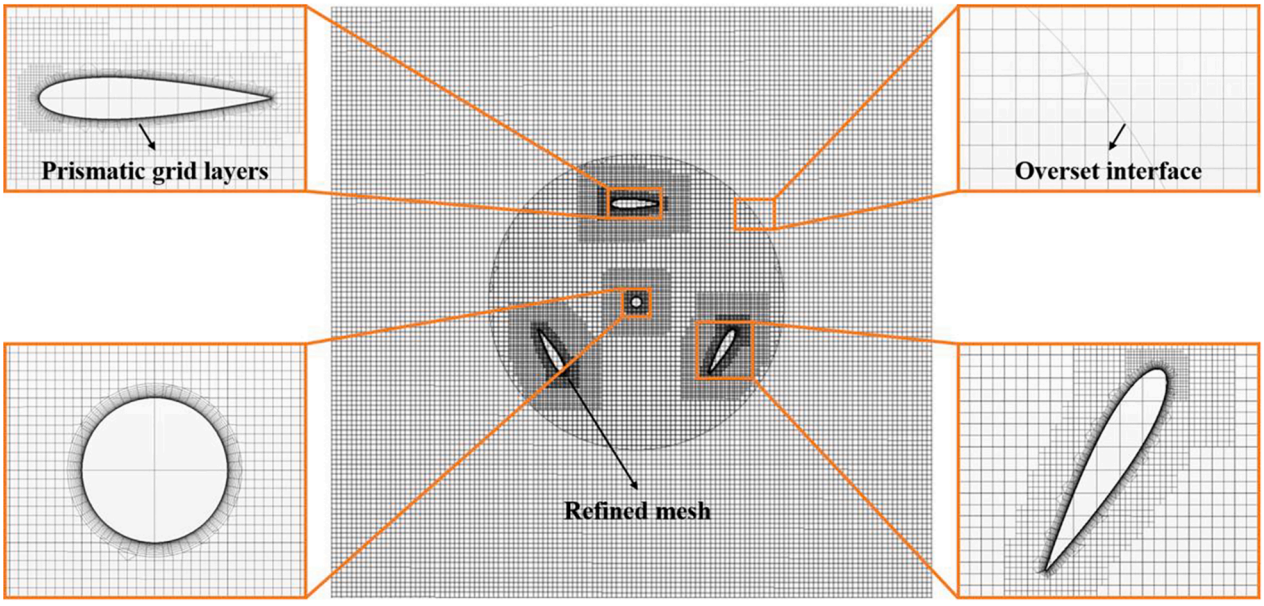

(b)

Fig. 4. Schematic of the mesh topology: (a) overall view; (b) mesh around the turbine.

Table 2
Solver settings.

Fluid flow modeling approach		Segregated flow model
Discretization scheme	Time	Implicit unsteady, 2nd-order
	Convection	Hybrid 2nd-order upwind/bounded central-differencing
Pressure-velocity coupling algorithm		SIMPLE
Physical time-step		$T/180$ (T denotes the period of one turbine revolution)
Maximum inner iteration		20

structures around the VAWTs will be visualized to obtain the underlying physical mechanism.
- Evaluating the effects of varied pitch characteristics on wake interference. For this purpose, the effects of the pitch amplitude and pitch period on the wake interference will be parametrically analyzed. Also, the power performance and wake pattern of the turbine array will be compared.

The contributions of the present study can be summarized in two aspects: (1) The wake interference between the offshore floating VAWTs is investigated for the first time. It should be noted that the systematic characterization of the effect of the platform pitch motion on the wake interference adds new knowledge to the design of offshore floating wind farms. (2) The detailed analysis of the power performance and wake pattern of the turbine array reveals the physical mechanism behind the effects of varied pitch characteristics on the wake interference, which

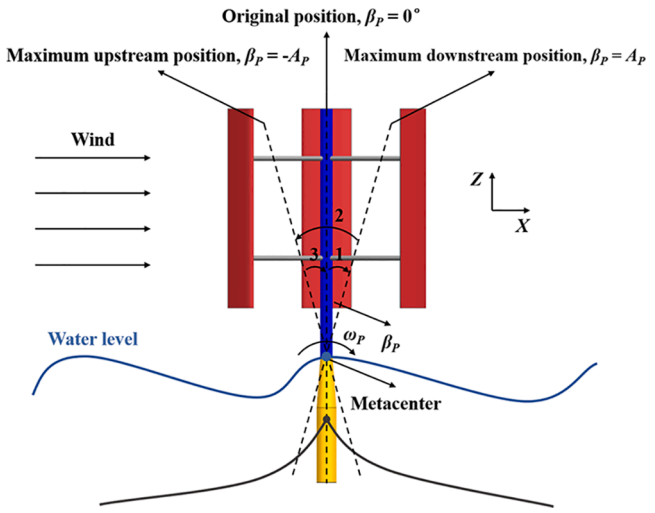

Fig. 5. Schematic of the offshore floating VAWT under the platform pitch motion. (Not to scale, floating platform and mooring lines are for illustration and are not considered in the simulations).

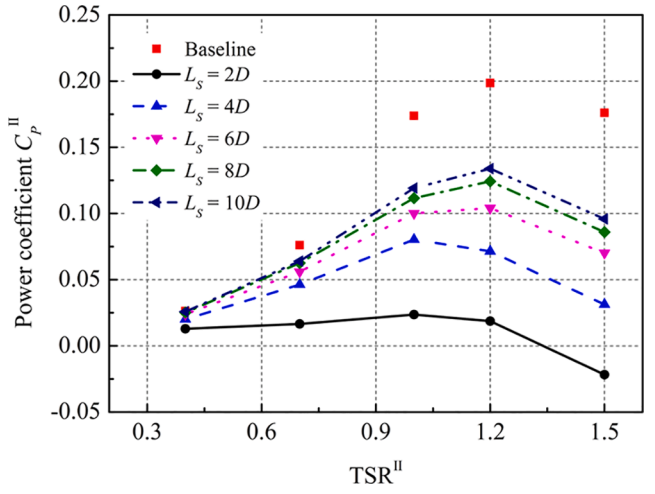

Fig. 6. Averaged power coefficients of VAWT II at different separation distances and TSR^{II}s when VAWT I is set to bottom-fixed. ($TSR^{I} = 1.2$).

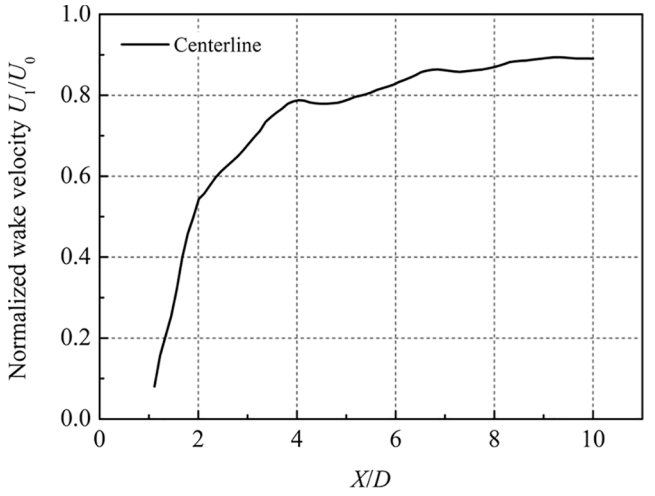

Fig. 7. Normalized mean wake velocity distribution of the bottom-fixed VAWT I along the centerline. ($TSR^{I} = 1.2$).

paves the way for future investigations of more complex scenarios.

The outline of the present study is as follows: Section 2 describes the geometric model of the offshore floating VAWTs. Section 3 details the employed numerical method. Section 4 characterizes the effect of the platform pitch motion on the wake interference within the turbine array. Section 5 provides the conclusions derived from the results and discussion. Section 6 points out the present limitations and gives a perspective for the future study.

2. Geometric model

Fig. 1 presents a schematic of the two tandem offshore floating VAWTs. The separation distance between the upstream turbine (VAWT I) and the downstream turbine (VAWT II) is denoted by L_S. Note that, in the present study, the aerodynamics and hydrodynamics of the VAWT system are uncoupled, and the floating platform and mooring lines are not considered in the simulations. The platform pitch motion is simplified to a series of prescribed sinusoidal functions, which is a common practice in the study of offshore floating wind turbines [34,40,41,42]. Also, a scaled land-based VAWT proposed by Elkhoury et al. [43] is selected for modeling the upper rotor. Table 1 lists the corresponding geometric features. It is noteworthy that the struts of the VAWT are neglected during the modeling process because they have a negligible impact on the turbine aerodynamics [44,45].

As the main operational parameter of the VAWTs, the TSR is defined as:

$$\mathrm{TSR} = \frac{\omega D}{2U_0} \tag{1}$$

where ω and U_0 are the angular and inflow velocities, respectively.

The typical aerodynamic parameters of the VAWTs, i.e., power coefficient C_P, torque coefficient C_Q, and thrust coefficient C_T, are computed as follows:

$$C_P = \frac{Q\omega}{\rho U_0{}^3 HD/2} \tag{2}$$

$$C_Q = \frac{Q}{\rho U_0{}^2 HD^2/4} \tag{3}$$

$$C_T = \frac{F_T}{\rho U_0{}^2 HD/2} \tag{4}$$

where ρ, Q, and F_T are the air density, torque, and thrust, respectively.

3. Numerical method

3.1. Turbulence modeling approach

In the present study, the SST k-ω IDDES is used for turbulence modeling in the commercial CFD software STAR-CCM+ 13.04. The SST k-ω IDDES combines the properties of the SST k-ω turbulence model in the boundary layers with the LES (Smagorinsky subgrid-scale model) in the unsteady separated regions [46]. According to the STAR-CCM+ User Guide [46] and the study of Shur et al. [47], the specific dissipation rate ω in the transport equations of the SST k-ω turbulence model is replaced by $\tilde{\omega}$, which is defined as:

$$\tilde{\omega} = \frac{\sqrt{k}}{l_{\mathrm{hyb}}\beta^* f_{\beta^*}} \tag{5}$$

where β^* is equal to 0.09 and f_{β^*} is the free-shear modification factor. Also, l_{hyb} denotes the length-scale of the SST k-ω IDDES, and is expressed as:

$$l_{\mathrm{hyb}} = \tilde{f}_d(1+f_e)l_{\mathrm{RANS}} + \left(1-\tilde{f}_d\right)l_{\mathrm{LES}} \tag{6}$$

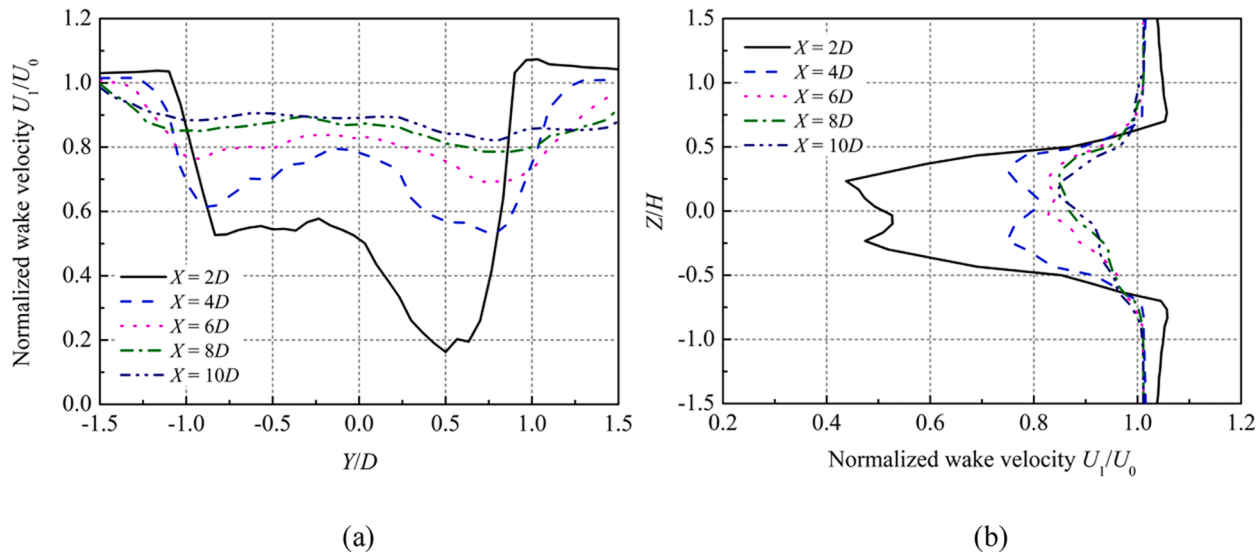

Fig. 8. Normalized mean wake profiles of the bottom-fixed VAWT I at different downstream distances: (a) *X-Y* plane; (b) *X-Z* plane. ($TSR^I = 1.2$).

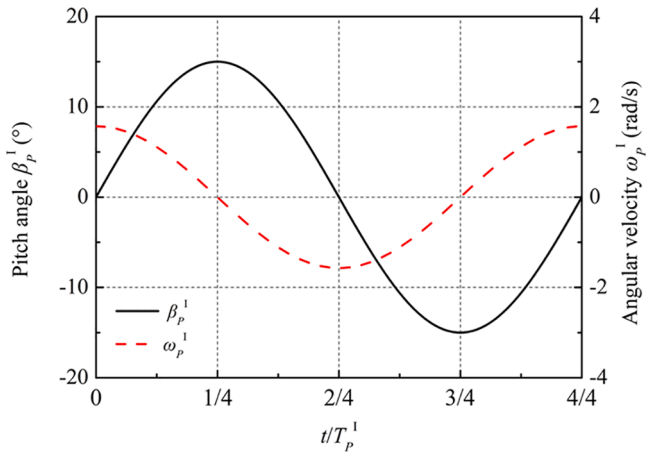

Fig. 9. Variations of the pitch angle and the corresponding angular velocity during one pitch period. ($A_P^I = 15°$, $T_P^I = 4T^I$).

$$\widetilde{f_d} = \max((1 - f_{dt}), f_B) \tag{7}$$

$$f_{dt} = 1 - \tanh\left[(C_{dt} r_{dt})^3\right] \tag{8}$$

$$f_B = \min\left[2\exp\left(-9\alpha^2\right), 1\right], \alpha = 0.25 - \frac{d_w}{h_{\max}} \tag{9}$$

$$f_e = \max\left[(f_{e1} - 1), 0\right]\psi f_{e2} \tag{10}$$

$$f_{e1} = \begin{cases} 2\exp(-11.09\alpha^2), \alpha \geq 0 \\ 2\exp(-9\alpha^2), \alpha < 0 \end{cases} \tag{11}$$

$$f_{e2} = 1 - \max(f_t, f_l) \tag{12}$$

$$f_t = \tanh\left[\left(C_t^2 r_{dt}\right)^3\right] \tag{13}$$

$$f_l = \tanh\left[\left(C_l^2 r_{dl}\right)^{10}\right] \tag{14}$$

$$r_{dt} = \frac{\nu_t}{\sqrt{\nabla \mathbf{u} : \nabla \mathbf{u}^T \kappa^2 d^2}}, \nu_t = \frac{\mu_t}{\rho} \tag{15}$$

$$r_{dl} = \frac{\nu}{\sqrt{\nabla \mathbf{u} : \nabla \mathbf{u}^T \kappa^2 d^2}} \tag{16}$$

where the blending function f_B and the elevating function f_e provide some capabilities of the wall-modeled LES (WMLES) to resolve the log-layer mismatch in detached-eddy simulation (DES). Also, d_w is the wall distance and $h_{\max}$ is the maximum local grid spacing. Ψ is the low-Reynolds number correction function and C_{dt}, C_t, and C_l are equal to 20, 1.87, and 5, respectively. In addition, ν is the kinematic viscosity, μ_t is the turbulent eddy viscosity, and κ is the von Karman constant, which is equal to 0.41. l_{RANS} and l_{LES} are the length-scales of the RANS method and LES, respectively. The SST k-ω IDDES adopts a new version of the subgrid length-scale Δ for l_{LES}, which relies on both wall distance and grid spacing. Note that Δ is computed as:

$$\Delta = \min(\max(0.15 d_w, 0.15 h_{\max}, h_{wn}), h_{\max}) \tag{17}$$

where h_{wn} is the grid spacing in the wall-normal direction.

The above modifications make the SST k-ω IDDES a powerful and balanced hybrid RANS/LES method for the complex turbulent flows at high Reynolds numbers, and has proven to be advantageous in predicting the aerodynamics and aeroacoustics of the wind turbines [48,49].

Fig. 2 presents a snapshot of the instantaneous flow pattern around the selected VAWT to visualize the RANS and LES regions. The DES upwind blending factor is employed to distinguish the computational regions. This factor is equal to one in attached shear layers and irrotational freestream flow regions, while it approaches zero in regions where LES is required, such as large-scale separated regions [46]. It can be seen that the DES upwind blending factor is equal to one in the thin boundary layer around the blade and in the irrotational flow region around the VAWT (RANS), and is close to zero in the unsteady separated region around the blade and in the core wake region (LES).

3.2. Computational domain

Fig. 3 presents a schematic of the computational domain employed in the present study. The domain consists of a fixed cuboid background region and two tandem cylindrical overset regions. The multi degrees of freedom motions of the VAWTs located in the overset regions are implemented by the overset mesh technique, in which the motion rules are prescribed using the user field function (UFF). The linear interpolation method is adopted to couple the solutions in the background region and the overset regions. Following the studies of Kuang et al. [20]

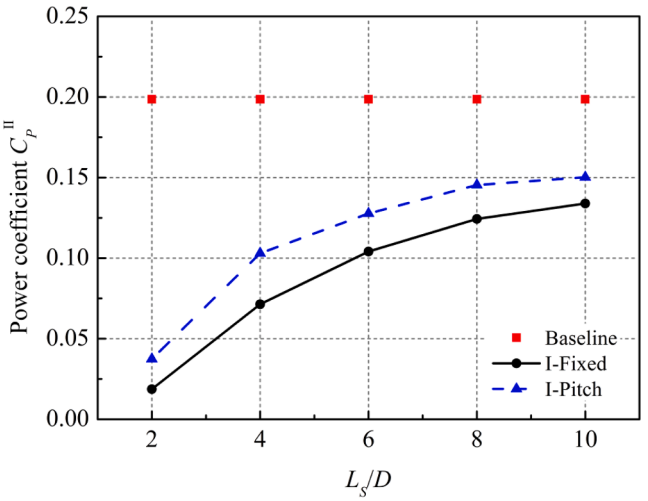

(a)

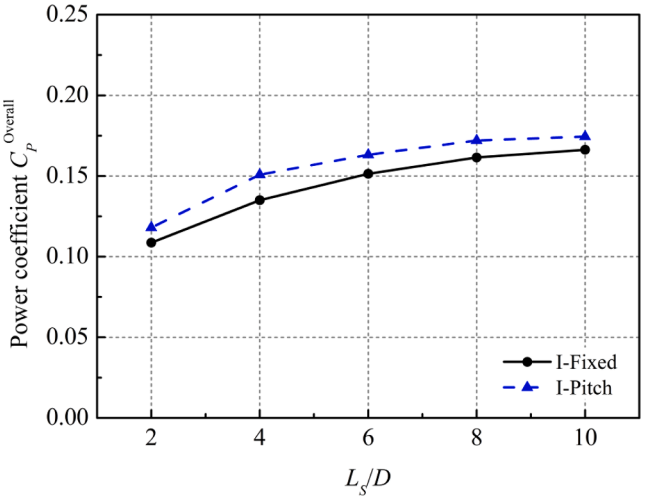

(b)

Fig. 10. Averaged power coefficients of the two VAWTs at different separation distances when VAWT I is under the platform pitch motion: (a) C_P^{II}; (b) $C_P^{Overall}$. ($TSR^I = TSR^{II} = 1.2$, $A_P^I = 15°$, $T_P^I = 4T^I$, $C_P^I = 0.2019$).

and Su et al. [50], the height E, width W, and length L of the domain are set to $5H$, $10D$, and $20D + L_S$, respectively. Also, the height and diameter of the overset regions are set to $1.5H$ and $1.5D$, respectively.

A uniform flow velocity of $U_0 = 8.0$ m/s is set at the inlet of the computational domain and a constant pressure of $P_0 = 0.0$ Pa is specified at the outlet. The corresponding turbulent velocity scale, turbulent viscosity ratio, and turbulence intensity are set to 1 m/s, 10, and 0.8%, respectively. It should be noted that the turbulence intensity is used to match the inflow condition of the wind tunnel tests [43], which is lower than that of the actual ocean environment. However, since the present study focuses on the physical mechanism behind the effect of the platform pitch motion, the main conclusions are still applicable. The effect of the turbulence intensity on the power and wake of the VAWTs has been investigated in the authors' previous study [20]. The other four boundaries of the domain are considered as the symmetry planes to avoid the boundary reflections [51]. The no-slip walls and overset interfaces are assigned to the VAWTs and overset regions, respectively.

3.3. Mesh topology and solver settings

Fig. 4 presents a schematic of the mesh topology employed in the present study. The computational domain is predominantly distributed with hexahedral grids. The mesh in the wake region and around the turbine is refined at different levels. High-resolution prismatic grids are generated near the blades and shaft to ensure accurate simulations of the boundary flows. In the case of the blades, for example, since the chord-based Reynolds number varies between 1.53×10^5 and 2.74×10^5 during the simulations, the growth rate, total thickness, and number of layers of the prismatic grid layers are set to 1.2, 7.2×10^{-3} m, and 27, respectively, to satisfy the requirement of $y^+ < 1$ for the SST k-ω IDDES [48]. The streamwise and spanwise grid spacings within the prismatic grid layers vary in the range of 6.25×10^{-4} m $- 1.25 \times 10^{-3}$ m. Therefore, the values of Δx^+ and Δz^+ are around 60 to 120, which match the IDDES tests of Shur et al. [47] and meet the simulation requirements of the hybrid RANS/LES method [52]. The validity of the mesh topology is thoroughly examined before the simulations and the report shows that 100% of the grids have a face validity of 1.0. Also, only 0.22% of the grids present a volume change of lower than 0.1, and the maximum skewness angle is 87.36°. The independence test of the mesh topology can be found in Supplementary reference S.1.

Table 2 lists the solver settings employed in the present study. These settings are based on the guidelines for transient analysis in the STAR-CCM+ User Guide [46], which have been proven to perform well in predicting the aerodynamics of the VAWTs [20,45]. The sensitivity test of the physical time-step and the solution validation of the numerical method can be found in Supplementary reference S.2 and S.3, respectively. The aerodynamic parameters of the VAWTs are sampled over one pitch period. When the changes in the averaged values of the parameters between two successive pitch periods drop below 0.2%, the computational convergence is considered to be achieved. Note that this convergence criterion is in agreement with the guidelines for CFD simulations of the VAWTs [53].

3.4. Prescribed platform pitch motion

In the present study, the platform pitch motion is assumed to follow a prescribed simple harmonic law with the given amplitudes A_P and periods T_P. Fig. 5 presents a schematic of the offshore floating VAWT under the platform pitch motion. The pitch angle β_P and the corresponding angular velocity ω_P are expressed as follows:

$$\beta_P = A_P \sin\left(\frac{2\pi}{T_P} t\right) \tag{8}$$

$$\omega_P = A_P \frac{2\pi}{T_P} \cos\left(\frac{2\pi}{T_P} t\right) \tag{9}$$

where t denotes the physical time. Note that the sequence of the platform pitch motion is defined as $1 \rightarrow 2 \rightarrow 3$, i.e., starting from the original position (OP) to the maximum downstream position (MDP), then pitching to the maximum upstream position (MUP) and returning to the OP. The rotation axis through the metacenter is in parallel with the Y-axis and is situated at the bottom of the overset region, i.e., $Z = -0.75H$.

4. Results and discussion

4.1. Wake interference between bottom-fixed turbines

In this subsection, the wake interference between the two tandem VAWTs, which are set to bottom-fixed, is investigated. The main purpose is, on the one hand, to explore the basic layout pattern of the bottom-fixed turbine array and, on the other hand, to provide a baseline for characterizing the effect of the platform pitch motion in the floating turbine array. The power performance of the downstream turbine (VAWT II, see Fig. 1) is the key object to be analyzed.

Fig. 6 shows the averaged power coefficients C_P^{II} of VAWT II at different separation distances L_S and TSR^{II}s. The upstream turbine

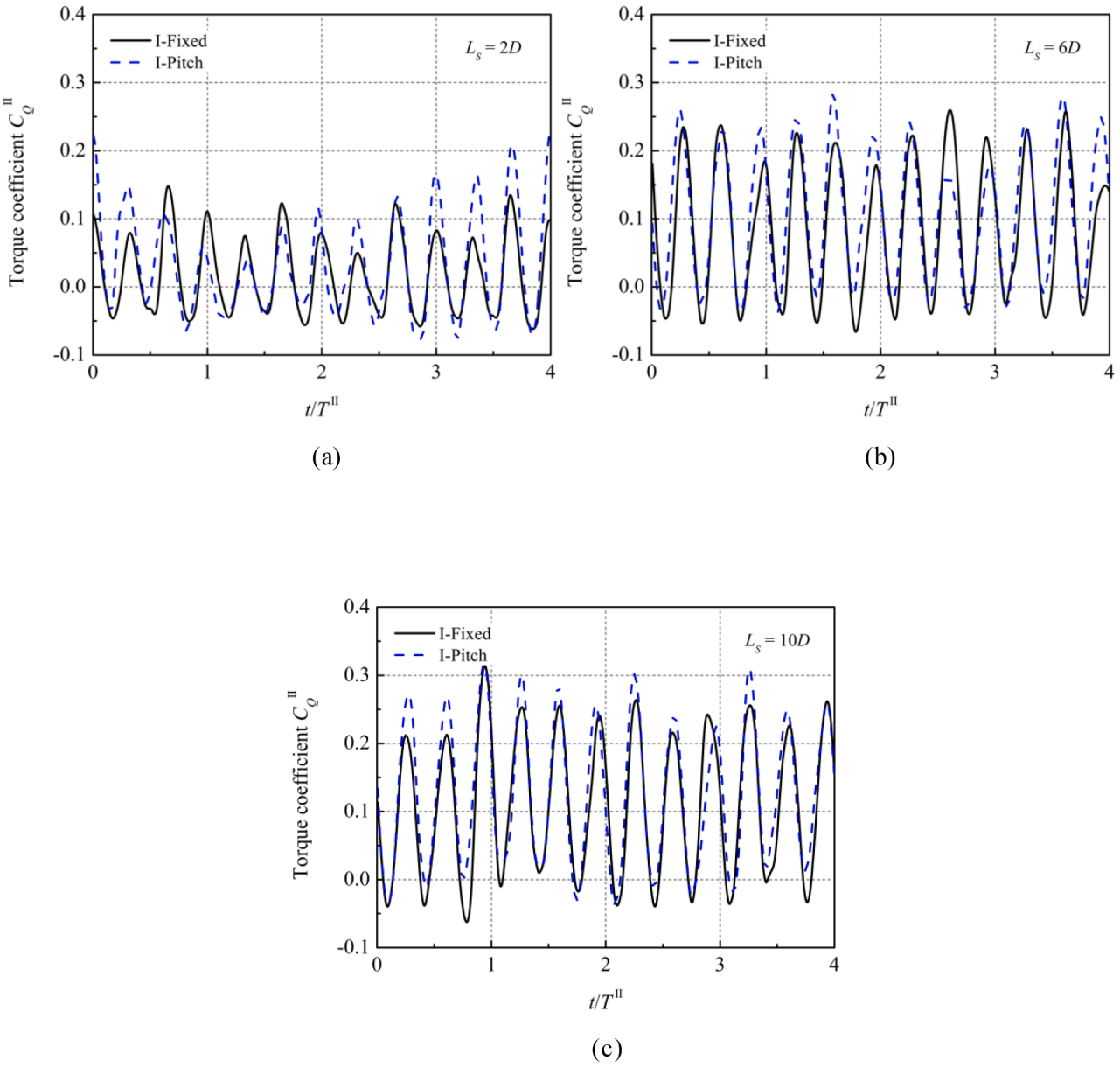

Fig. 11. Instantaneous torque coefficients of VAWT II at different separation distances when VAWT I is under the platform pitch motion: (a) $L_S = 2D$; (b) $L_S = 6D$; (c) $L_S = 10D$. ($TSR^I = TSR^{II} = 1.2$, $A_P{}^I = 15°$, $T_P{}^I = 4T^I$).

(VAWT I) is operating at an optimal TSR^I of 1.2. The baseline values refer to C_P of the isolated bottom-fixed VAWTs. It can be seen that due to the strong wake interference and large velocity deficit in the wake region of VAWT I, the power performance of VAWT II noticeably deteriorates at moderate and high TSR^{II}s. When VAWT II is located in the near wake region ($L_S = 2D$), the peak value of $C_P{}^{II}$ decreases from 0.1986 to 0.0236, which is 11.88% of the baseline value. As L_S increases, the power performance of VAWT II gradually picks up and the optimal TSR^{II} rises correspondingly, which is in agreement with the results of Dessoky et al. [54]. The peak value of $C_P{}^{II}$ reaches 52.42% of the baseline value when VAWT II is located in the medium wake region, i.e., $L_S = 6D$. However, the performance improvement diminishes with the further increase of L_S, meaning that the absolute increments of $C_P{}^{II}$ from $L_S = 6D$ to $8D$ and from $L_S = 8D$ to $10D$ are 0.0202 and 0.0096, respectively. Therefore, it makes little sense to locate VAWT II in the far wake region ($L_S > 8D$), where the performance improvement is limited and the space cost of the turbine array will increase.

To explain the above physical phenomena, Fig. 7 shows the normalized mean wake velocity distribution of the bottom-fixed VAWT I along the centerline ($Y = 0$, $Z = 0$, see Fig. 1). It can be seen that the variation of the wake velocity has distinct regional characteristics: In the near wake region ($L_S < 2D$), the velocity deficit is relatively large and the wake recovers rapidly. In the transitional wake region ($2D < L_S < 4D$), the wake recovery slows down slightly and the velocity deficit is reduced to 21.22% at $L_S = 4D$, which corresponds to the pronounced increment of $C_P{}^{II}$ shown in Fig. 6; The wake recovery enters a placid state in the medium wake region ($4D < L_S < 8D$) and presents some fluctuations. These fluctuations can be explained by the inherent developing mechanism of the turbine wake [20], in which the small-scale shedding vortices gradually merge into large-scale vortices, enhancing the exchange of the momentum between the ambient air and the turbine wake. In the far wake region ($L_S > 8D$), corresponding to the limited performance improvement shown in Fig. 6, the wake recovery is quite slow, with the wake velocities at $L_S = 8D$ and $10D$ reaching 87.28% and

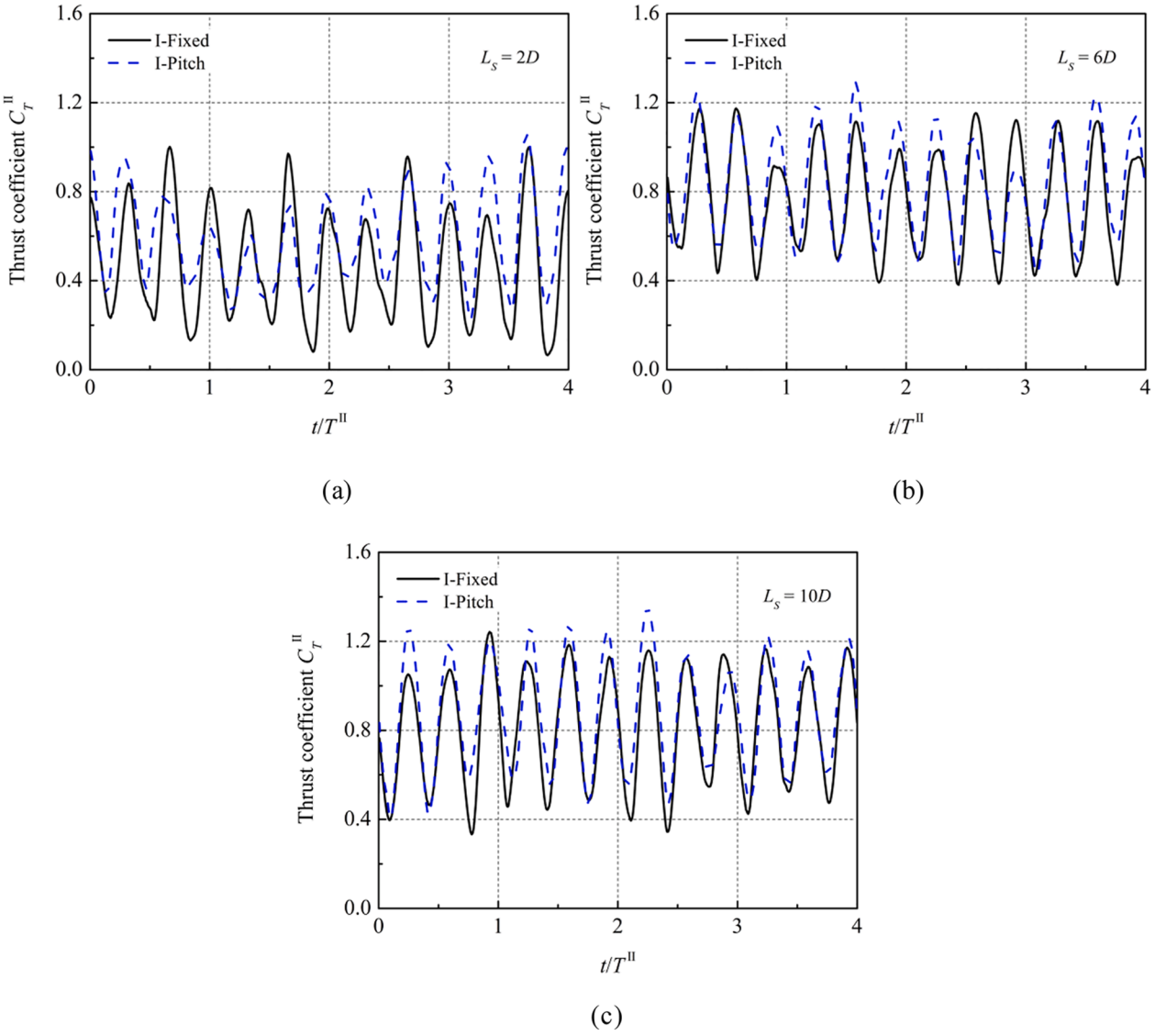

Fig. 12. Instantaneous thrust coefficients of VAWT II at different separation distances when VAWT I is under the platform pitch motion: (a) $L_S = 2D$; (b) $L_S = 6D$; (c) $L_S = 10D$. ($TSR^{I} = TSR^{II} = 1.2$, $A_P^{I} = 15°$, $T_P^{I} = 4T^{I}$).

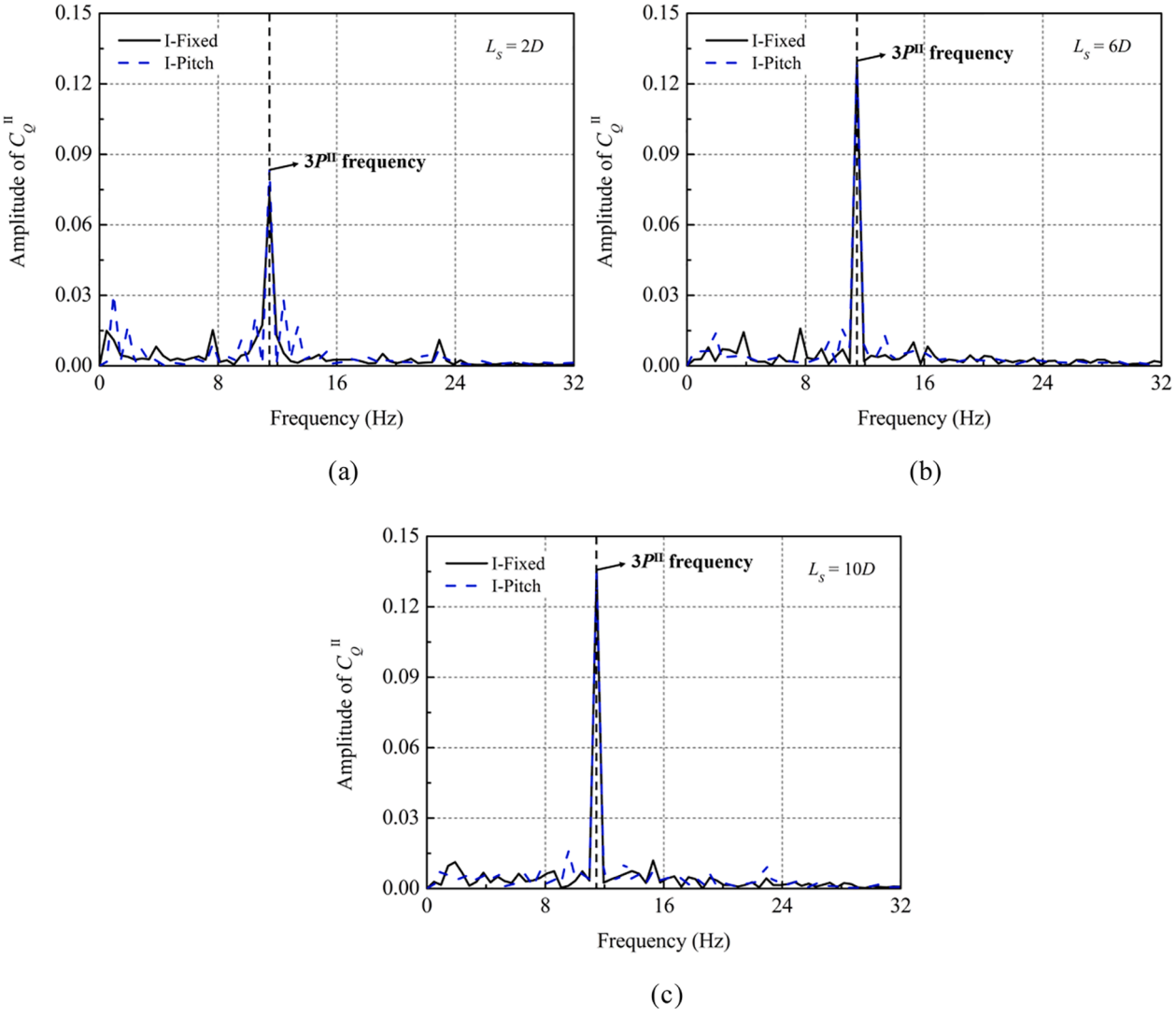

Fig. 13. Spectra of the instantaneous torque coefficients of VAWT II at different separation distances when VAWT I is under the platform pitch motion: (a) $L_S = 2D$; (b) $L_S = 6D$; (c) $L_S = 10D$. ($TSR^{I} = TSR^{II} = 1.2$, $A_P{}^{I} = 15°$, $T_P{}^{I} = 4T^{I}$).

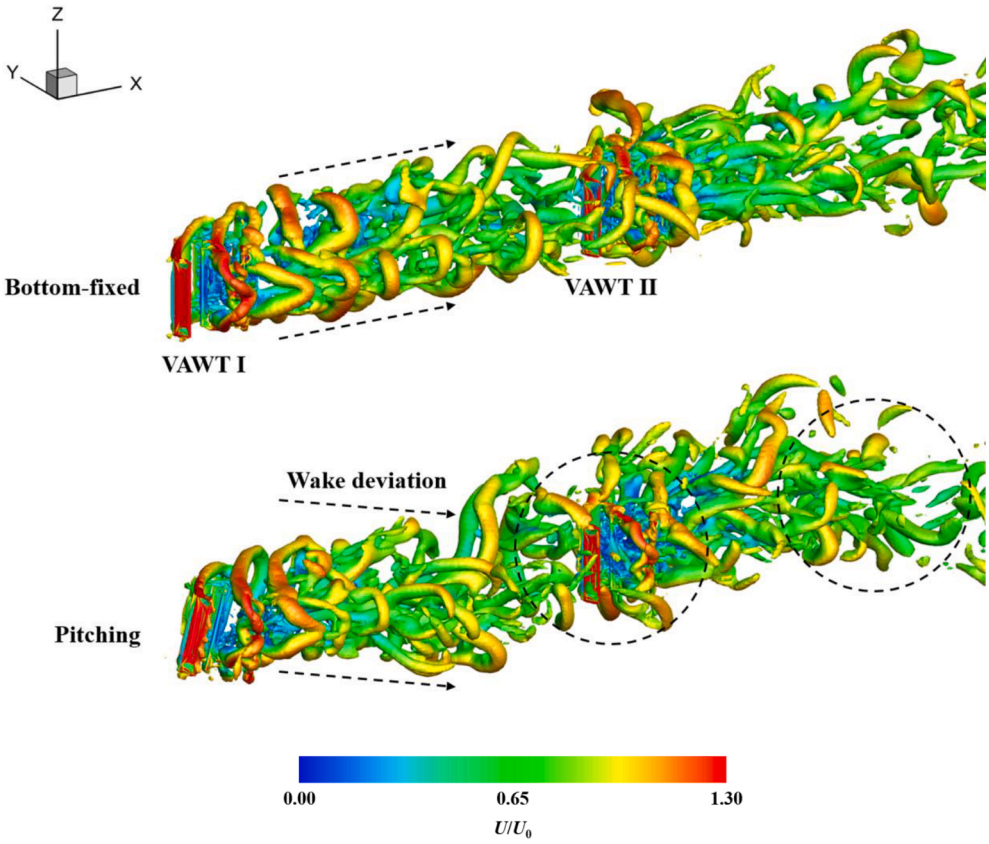

Fig. 14. Instantaneous vortical structures around the two VAWTs at $L_S = 6D$ when VAWT I pitches to the MDP. ($TSR^{I} = TSR^{II} = 1.2$, $A_P{}^{I} = 15^{\circ}$, $T_P{}^{I} = 4T^{I}$).

89.07% of the inflow velocity, respectively. In addition, Fig. 8 shows the normalized mean wake profiles of the bottom-fixed VAWT I at different downstream distances. Below are the observed phenomena:

- The Magnus effect [55] causes the turbine wake to deviate from the centerline in the *X-Y* plane, and this phenomenon gradually diminishes as the wake develops.
- As the downstream distance increases, the influence range of the turbine wake continues to expand, the wake profile becomes smoother, and the reduction of the velocity deficit decreases.
- When $L_S > 6D$, the variation of the turbine wake is not pronounced, especially in the *X-Z* plane, where the wake profiles are nearly identical.

The above results and discussion show that locating VAWT II in the medium wake region of VAWT I can appropriately balance the power performance and space cost of the bottom-fixed turbine array. It should be noted that the high-solidity characteristic of the selected VAWT and the Reynolds number scaling effect (RNSE) [56] may lead to an uncritical estimation of the wake recovery, thereby giving a rough division of the wake region. Nevertheless, the present findings are still relevant for the full-scale VAWTs with low and moderate solidities.

4.2. Wake interference between turbines under platform pitch motion

In this subsection, the wake interference between the pitching VAWT I and the bottom-fixed VAWT II is investigated. As described in Section 3.4, the platform pitch motion of VAWT I follows a prescribed simple harmonic law. The pitch amplitude $A_P{}^{I}$ and pitch period $T_P{}^{I}$ are set to 15° and $4T^{I}$, respectively, in which T^{I} is one revolution period of VAWT I. The variations of the pitch angle $\beta_P{}^{I}$ and the corresponding angular velocity $\omega_P{}^{I}$ during one pitch period are shown in Fig. 9. The selection of the values of $A_P{}^{I}$ and $T_P{}^{I}$ is based on two principles: The oscillation amplitude of the platform should not exceed the safety limit, and the natural motion frequency (period) of the platform ought to be safely away from the typical range of the wave frequency (period).

Fig. 10 shows the averaged power coefficients $C_P{}^{II}$ of VAWT II and the averaged power coefficients $C_P{}^{Overall}$ of the turbine array at different separation distances L_S. $C_P{}^{Overall}$ is calculated as the arithmetic mean of $C_P{}^{I}$ and $C_P{}^{II}$. Note that both VAWTs are operating at the same TSR of 1.2. It can be seen that the power performance of VAWT II is significantly improved when VAWT I is under the platform pitch motion, e.g., the relative increment of $C_P{}^{II}$ at $L_S = 6D$ reaches 22.67%. The power performance of the turbine array is improved correspondingly, with a relative increment of 7.79% in $C_P{}^{Overall}$ at $L_S = 6D$. The slight increase in $C_P{}^{I}$ from 0.1986 to 0.2019 also contributes to this improvement. These indicate that, on the one hand, the floating VAWT array can achieve a higher power output compared to the bottom-fixed one. On the other hand, while ensuring a sufficient separation distance required for safety (e.g., avoiding the mooring line interference), the offshore floating VAWTs can be arranged more closely to reduce the space cost of the wind farm and increase its installed capacity.

Fig. 11 shows the instantaneous torque coefficients $C_Q{}^{II}$ of VAWT II within four turbine revolutions (one pitch period of VAWT I) at three typical separation distances, i.e., $L_S = 2D$, $6D$, and $10D$, which correspond to the near wake region, medium wake region, and far wake region, respectively. It can be seen that at $L_S = 2D$, the peak values of $C_Q{}^{II}$ during the physical time t of $(0, 1/2T^{II})$ and $(2T^{II}, 4T^{II})$ are significantly increased when VAWT I is under the platform pitch motion. Note that these pronounced increments compensate for the decreases of the peak value of $C_Q{}^{II}$ at $t = (1/2T^{II}, 2T^{II})$ and the negative increases of the valley value at $t = (5/2T^{II}, 7/2T^{II})$. Thus, the value of $C_P{}^{II}$ increases by 100%. Moreover, more intense fluctuations are observed in the variation of $C_Q{}^{II}$, which is similar to the condition of the isolated pitching VAWTs [40,50]. It should be noted that the increase of L_S changes the effect of the platform pitch motion on $C_Q{}^{II}$. For example, the peak and valley

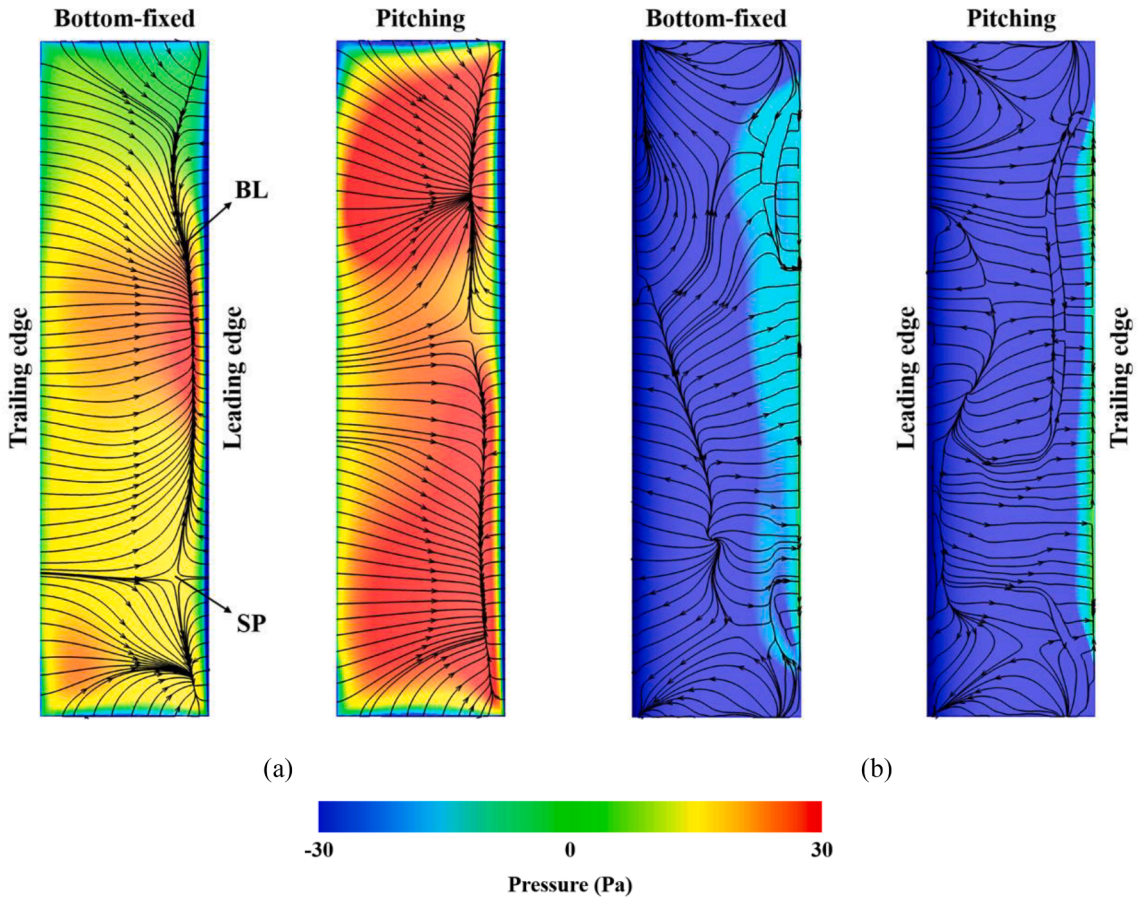

Fig. 15. Instantaneous pressure and streamline distributions on blade 2-II when VAWT I pitches to the MDP: (a) pressure side; (b) suction side. (BL: bifurcation line, SP: saddle point, $TSR^{I} = TSR^{II} = 1.2$, $A_P{}^{I} = 15°$, $T_P{}^{I} = 4T^{I}$).

values of $C_Q{}^{II}$ are increased in nearly all intervals of $t = (0, 4T^{II})$ at $L_S = 10D$, and the fluctuations of $C_Q{}^{II}$ diminish. As shown in Fig. 12, the effect of the platform pitch motion of VAWT I on the thrust coefficients $C_T{}^{II}$ of VAWT II is the same as its effect on $C_Q{}^{II}$. It implies that the peak and valley values of $C_T{}^{II}$ are generally increased. It should be noted that the fluctuations of $C_Q{}^{II}$ and $C_T{}^{II}$ are attributed to the upstream wake variation induced by the platform motion and the strong instability inherent in the wake of the high-solidity VAWT I [17]. This phenomenon is also reported by Rezaeiha et al. [37] and Zuo et al. [19]. Overall, the enlarged aerodynamic load undoubtedly contributes to the performance improvement of VAWT II. However, it also introduces some structural problems, e.g., vibration and fatigue.

Fig. 13 shows the spectra of the instantaneous torque coefficients $C_Q{}^{II}$ of VAWT II at different separation distances L_S. The fast Fourier transform (FFT) technique is employed to analyze the time series of $C_Q{}^{II}$ during four pitch periods to obtain the amplitude spectra. It can be seen that the platform pitch motion of VAWT I will not change the main spectral features of $C_Q{}^{II}$ because peaks are found evidently at the $3P^{II}$ frequency (11.46 Hz), in which P^{II} (3.82 Hz) is the rotating frequency of VAWT II. However, Rezaeiha et al. [37] observed visible peaks in the power spectra of the instantaneous C_P of the downstream HAWT at the surge frequency of the upstream HAWT. Note that these two contradictory phenomena reveal the different aerodynamic characteristics of the HAWTs and VAWTs. Specifically, the $n \times P$ criterion dominates the spectral features of the VAWTs, while those of the HAWTs are more sensitive to the oscillation frequencies of the platforms. Besides, when VAWT I is under the platform pitch motion, the peak amplitudes of $C_Q{}^{II}$ slightly increase, which corresponds to the intense fluctuations shown in Fig. 11.

To explore the physical mechanism behind the effect of the platform pitch motion on the wake interference, Fig. 14 illustrates the instantaneous vortical structures around the two VAWTs at $L_S = 6D$ when VAWT I pitches to the MDP (see Figs. 5 and 9, at $t = 1/4T_P{}^{I}$). The *Q*-criterion is employed for the vortex identification and the velocity magnitude is adopted to tint the *iso*-surfaces. It can be seen that the wake trajectory of the pitching VAWT I significantly deviates from the centerline along the negative *Z*-direction compared to that of the bottomed-fixed one. This characteristic enables VAWT II to partially avoid the wake interference from VAWT I and experience a higher inflow velocity, which corresponds to the pronounced performance improvement shown in Fig. 10. Besides, the platform pitch motion complicates the wake field of VAWT I, which enhances the blade-vortex interaction of VAWT II, leading to more intense fluctuations in the instantaneous aerodynamic loads (see Fig. 11(b) and Fig. 12(b)). Fig. 15 illustrates the pressure and streamline distributions on blade 2-II (see Fig. 1). When VAWT I is under the platform pitch motion, on the one hand, the pressure difference between the pressure side and suction side of blade 2-II is significantly increased, which corresponds to the enlarged inflow velocity and aerodynamic load. On the other hand, the flow pattern on blade 2-II is changed, especially on the suction side, where the bifurcation line moves toward the leading edge, indicating an earlier onset of the flow separation. As a result of the enhanced blade-vortex interaction, the streamline distribution on the suction side of blade 2-II is found to be more chaotic, with several observed saddle points, reflecting the growth of the complex cross-flow structures along the spanwise direction. The platform pitch motion also disrupts the regular wake development of VAWT II, implying the premature breakage of the wake structure. This point is confirmed by Fig. 16, in which the comparison of the mean wake velocity fluctuations is illustrated. Fig. 16 shows that the fluctuating amplitude and range of the wake velocity of both VAWTs are

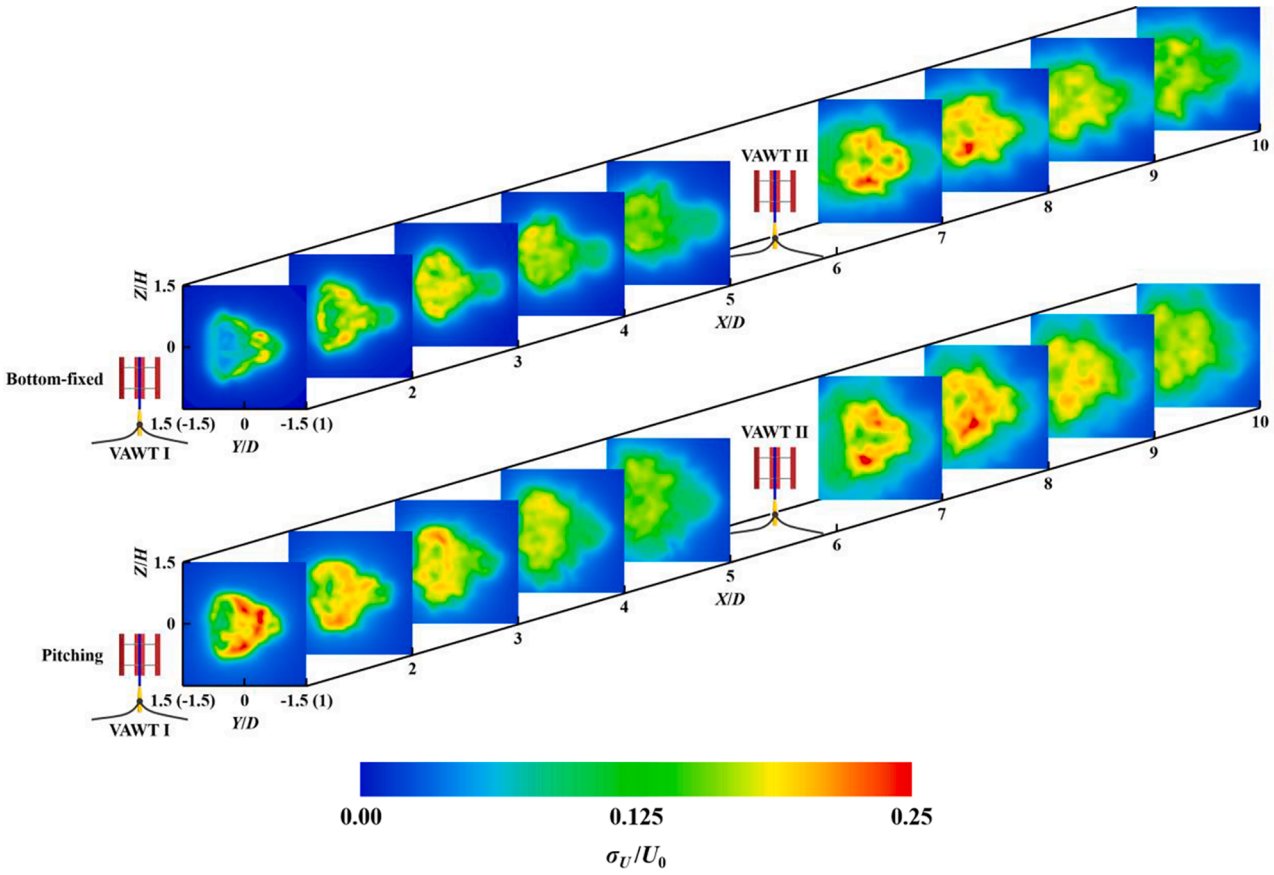

Fig. 16. Mean wake velocity fluctuations of the two VAWTs in the *Y-Z* plane at different downstream distances. ($TSR^{I} = TSR^{II} = 1.2$, $A_P{}^{I} = 15°$, $T_P{}^{I} = 4T^{I}$).

significantly enlarged when VAWT I is under the platform pitch motion. It should be noted that the flow field around the two VAWTs is sampled over one pitch period. When the change in the mean wake profile at $X = 10D$ between two successive pitch periods is fairly small (relative difference of the mean wake velocity at the centerline drops below 0.2%), the flow field is considered to have converged and its mean values can be monitored. Note that the wake velocity fluctuations are calculated by $\sigma_U = \sqrt{\frac{1}{3}(u'^2 + v'^2 + w'^2)}$, in which u', v', and w' are the local velocity fluctuations in the *X*-, *Y*-, and *Z*-directions, respectively.

Fig. 17 illustrates the instantaneous flow patterns around the two VAWTs in the *X-Z* plane at four typical moments, i.e., $t = 1/4T_P{}^{I}$, $2/4T_P{}^{I}$, $3/4T_P{}^{I}$, and $4/4T_P{}^{I}$, which correspond to the MDP, OP, MUP, and OP of VAWT I, respectively. Fig. 17 shows that the wake pattern of VAWT I is highly dependent on the platform pitch motion, in which the core wake region alternately appears below and above the centerline as the pitch position changes. The wake trajectory of VAWT I presents vertical deviations at different moments, especially at $t = 1/4T_P{}^{I}$ and $3/4T_P{}^{I}$. At these moments, when VAWT I pitches to the corresponding extreme positions, the wake trajectory has the maximum deviation exceeding the blade span length. On the one hand, the wake deviation induced by the platform pitch motion can alleviate the negative effect of the wake interference on the power performance of VAWT II. On the other hand, it can change the wake pattern of VAWT II (e.g., expanding the influence range) and promote the wake of the turbine array to spread in a wave-like manner to the downstream region. In other words, the platform pitch motion of VAWT I not only can contribute to the performance improvement of VAWT II but also may be beneficial to the VAWTs farther downstream.

As mentioned above, the platform pitch motion has a considerable impact on the wake pattern of VAWT I (e.g., deviating the wake trajectory), which is expected to noticeably change the corresponding wake profiles. Fig. 18 shows the normalized mean wake profiles of the pitching VAWT I in the *X-Z* plane at different downstream distances. It can be seen that when VAWT I is under the platform pitch motion, the mean velocity deficit in its core wake region ($-0.5 \le Z/H \le 0.5$) is noticeably reduced at any downstream distance, while the influence range of the turbine wake is expanded, especially in the far wake region. These can be explained as follows:

- The periodic wake deviation induced by the platform pitch motion spreads part of the velocity deficit outside the core wake region, i.e., $Z < -0.5H$ and $Z > 0.5H$.
- As illustrated in Fig. 17, the maximum deviation of the wake trajectory gradually enlarges with the increase of the downstream distance, which is also reported by Lei et al. [36].

Overall, the platform pitch motion can reduce the mean velocity deficit in the core wake region of VAWT I by deviating the wake trajectory, which is proven to improve the power performance of VAWT II. However, the application of some spatial strategies for reducing the wake interference between tandem offshore wind turbines may be limited by the expanded influence range of the turbine wake, e.g., vertically-staggered arrangement [57,58].

4.3. Effects of pitch amplitude and pitch period

The hydrodynamics of the floating structures are sensitive to sea state variations. Different wind and wave conditions will result in distinct motion characteristics of the platforms [40]. Thus, in this subsection, the effects of the pitch amplitude, $5° \le A_P{}^{I} \le 15°$, and pitch period, $2T^{I} \le T_P{}^{I} \le 8T^{I}$, on the wake interference between the pitching VAWT I and the bottom-fixed VAWT II are characterized. The selection of the values of $A_P{}^{I}$ and $T_P{}^{I}$ is based on the studies of Lei et al. [36,40],

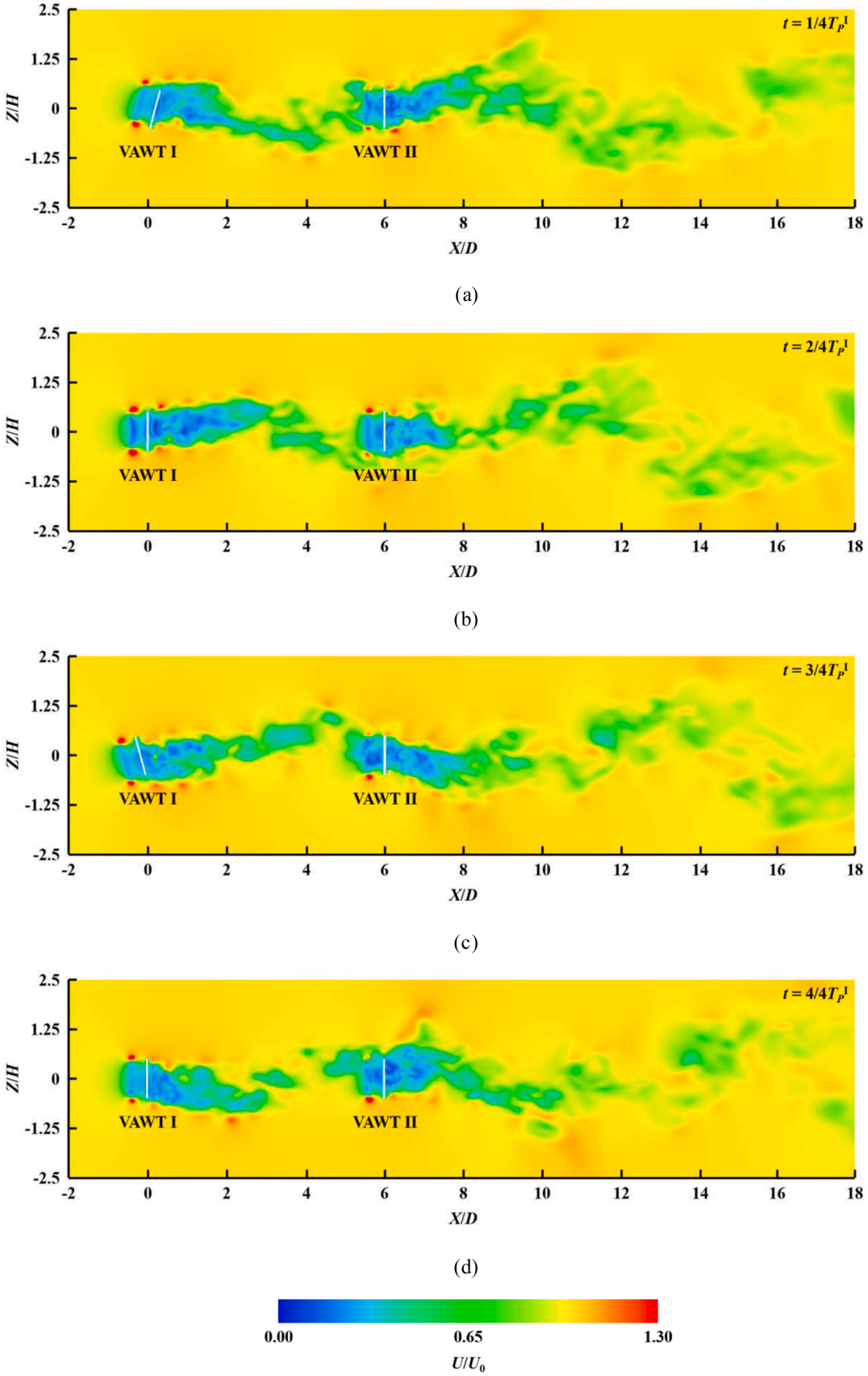

Fig. 17. Instantaneous flow patterns around the two VAWTs in the *X-Z* plane at different moments when VAWT I is under the platform pitch motion: (a) $t = 1/4T_P^{I}$; (b) $t = 2/4T_P^{I}$; (c) $t = 3/4T_P^{I}$; (d) $t = 4/4T_P^{I}$. ($L_S = 6D$, $TSR^{I} = TSR^{II} = 1.2$, $A_P{}^{I} = 15°$, $T_P{}^{I} = 4T^{I}$).

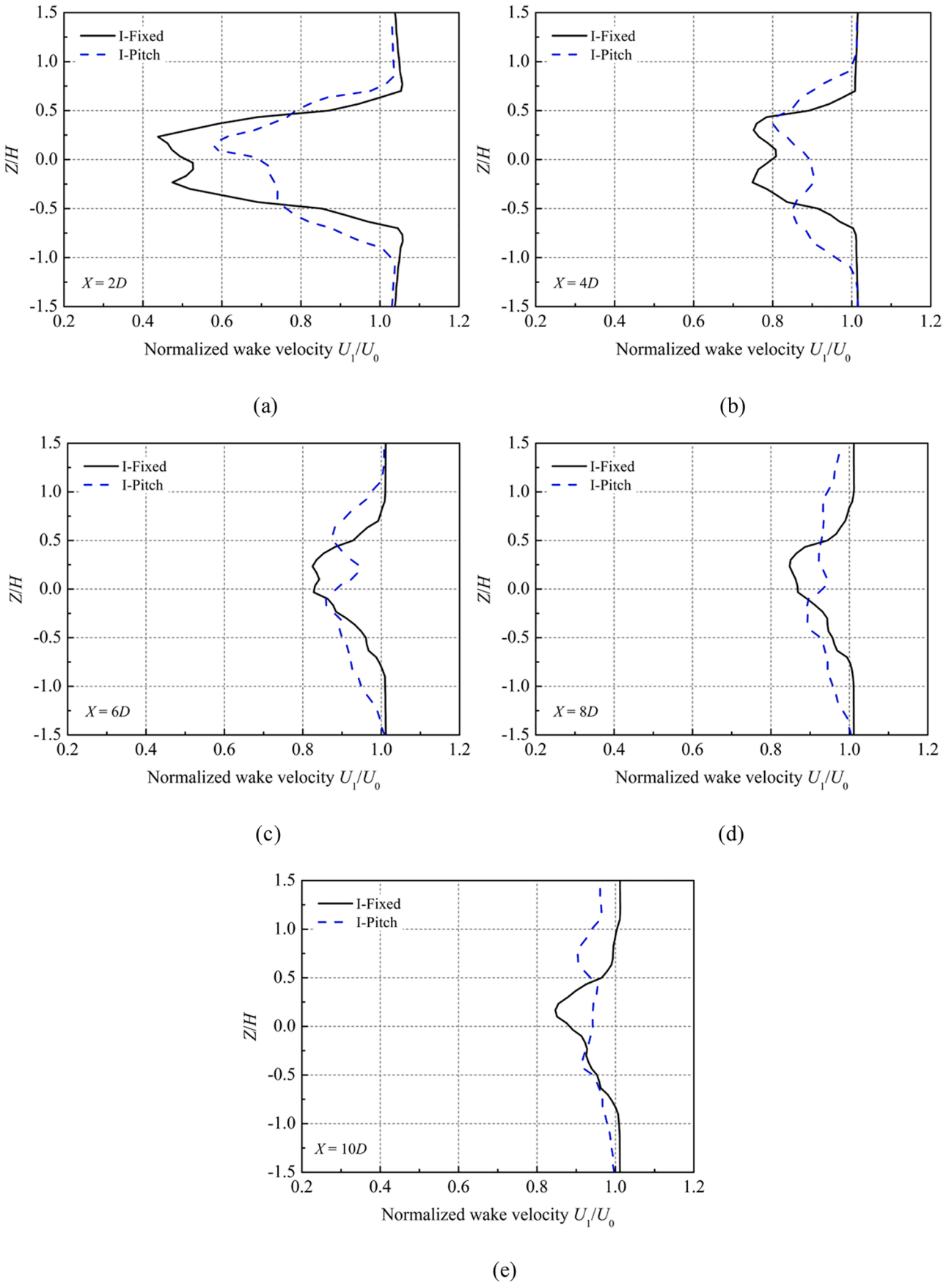

Fig. 18. Normalized mean wake profiles of the pitching VAWT I in the *X-Z* plane at different downstream distances: (a) $X = 2D$; (b) $X = 4D$; (c) $X = 6D$; (d) $X = 8D$; (e) $X = 10D$. ($TSR^{I} = TSR^{II} = 1.2$, $A_P^{I} = 15°$, $T_P^{I} = 4T^{I}$).

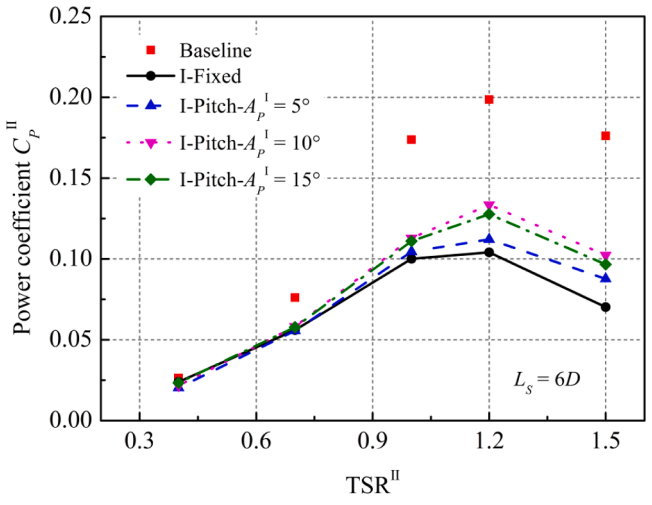

Fig. 19. Averaged power coefficients of the two VAWTs for different pitch amplitudes: (a) C_P^{II}; (b) $C_P^{Overall}$. ($L_S = 6D$, $TSR^I = 1.2$, $T_P^I = 4T^I$, $C_P^I = 0.1993$, 0.2007, and 0.2019 for $A_P^I = 5°$, 10°, and 15°, respectively).

Wen et al. [41], Fang et al. [42], Su et al. [50], and Tran et al. [34], following both principles described in Section 4.2. Specifically, on the one hand, the pitch amplitude of the platform does not exceed the safety limit of 15° suggested by Collu et al. [59]. On the other hand, the pitch period range of the scaled VAWT (platform) is 0.524 ~ 2.094 s (T^I = 0.262 s, corresponding to $TSR^I = 1.2$), and the Froude scaling ratio is assumed to be 1:100. Thus, the range of the excitation pitch period of the full-scale VAWT (platform) is 5.236 ~ 20.944 s, which falls within the typical range of the wave period of 5 ~ 20 s and is safely away from the natural pitch period of the platform, e.g., 25.8 s [60].

Fig. 19 shows the averaged power coefficients C_P^{II} of VAWT II and the averaged power coefficients $C_P^{Overall}$ of the turbine array for different pitch amplitudes A_P^I. Note that the pitch period T_P^I is fixed to $4T^I$. and the separation distance L_S is set to 6D, where VAWT II is located in the medium wake region of VAWT I. Fig. 19 shows that the platform pitch motion of VAWT I can considerably improve the power performance of VAWT II at moderate and high TSR^{II}s. However, there is nearly no difference at low TSR^{II}s, and the turbine performance for $A_P^I = 5°$ is even inferior to that of the bottom-fixed one when TSR^{II} is equal to 0.4. As A_P^I increases, the performance improvement of VAWT II becomes more pronounced, e.g., the relative increments of the peak value of C_P^{II} at $A_P^I = 5°$ and 10° are 7.68% and 22.67%, respectively. Somewhat surprisingly, the power performance of VAWT II slightly deteriorates when A_P^I further increases from 10° to 15°, in which the peak value of C_P^{II} drops from 0.1335 to 0.1277. Besides, as the value of C_P^I gradually increases with the increase of A_P^I, the power performance of the turbine array presents further improvement, and the negative effect of the excessively large A_P^I is alleviated. Specifically, the peak values of $C_P^{Overall}$ for $A_P^I = 10°$ and 15° are 0.1671 and 0.1648, respectively, which are considerably close.

To explain the above physical phenomena, Fig. 20 illustrates the instantaneous flow patterns around the two VAWTs in the *X-Z* plane for different pitch amplitudes A_P^I when VAWT I pitches to the MDP. It can be seen that the wake deviation induced by the platform pitch motion enlarges with the increase of A_P^I, which enables VAWT II to avoid more wake interference and experience a higher inflow velocity, thereby achieving a higher power output. However, since the blade aerodynamics of the VAWTs are strongly affected by the unsteady flow separation and dynamic stall at low TSRs [61,62], the improvement of the turbine performance from higher inflow velocities will be limited. The nearly identical values of C_P^{II} for $L_S \geq 6D$ at $TSR^{II} = 0.4$, which is shown in Fig. 6 also confirm this point. Besides, as mentioned in Section 4.2, the complex flow field of the pitching VAWT I will enhance the blade-vortex interaction of VAWT II, and this may lead to the premature onset of the dynamic stall and negatively affect the turbine performance, which corresponds to the decreased value of C_P^{II} for $A_P^I = 5°$ at $TSR^{II} = 0.4$.

Fig. 21 shows the normalized instantaneous wake profiles of the pitching VAWT I in the *X-Z* plane at four typical moments for different pitch amplitudes A_P^I. At $t = 1/4T_P^I$, when VAWT I pitches to the MDP, the velocity deficit in the core wake region for $A_P^I = 5°$ is larger than that for $A_P^I = 10°$ and 15°. This is because the wake deviation for $A_P^I = 5°$ is relatively small, and most of the velocity deficit stays in the core wake region rather than spreading outward. Meanwhile, the wake velocity for $A_P^I = 10°$ is found to be generally higher than that for $A_P^I = 15°$, which corresponds to the larger values of C_P^{II}, as shown in Fig. 19. This can be justified by the findings of Lei et al. [36]: Although the platform pitch motion can deviate the turbine wake and reduce the wake interference, it will enlarge the velocity deficit along the wake trajectory, which is more pronounced for the larger pitch amplitudes, thereby diminishing the benefit of the wake deviation. When VAWT I returns to the OP (see Fig. 21(b) and (d)), the wake trajectory moves toward the centerline. This movement promotes the enlargement of the velocity deficit in the core wake region. Therefore, the wake velocity for $A_P^I = 10°$ or 15° is lower than that for $A_P^I = 5°$, especially at $t = 4/4T_P^I$.

Fig. 22 shows the averaged power coefficients C_P^{II} of VAWT II and the averaged power coefficients $C_P^{Overall}$ of the turbine array for different pitch periods T_P^I. The pitch amplitude A_P^I is fixed to 15° and the separation distance L_S is set to 6D. It can be seen that the power performance of VAWT II keeps improving as T_P^I decreases, in which the peak value of C_P^{II} for $T_P^I = 2T^I$ reaches 73.11% of the baseline value. The smaller T_P^I is found to bring a more pronounced improvement in the turbine performance. It means that the relative increments of the peak value of C_P^{II} from $T_P^I = 8T^I$ to $4T^I$ and from $T_P^I = 4T^I$ to $2T^I$ are 5.02% and 13.70%, respectively. This phenomenon is also observed for the isolated pitching VAWTs in the studies of Lei et al. [40] and Su et al. [50]. Besides, the value of C_P^I is found to significantly increases as T_P^I decreases, which brings the peak value of $C_P^{Overall}$ of the floating turbine array for $T_P^I = 2T^I$ to about 120% of that of the bottom-fixed one. However, since the value of C_P^I for $T_P^I = 8T^I$ drops to 0.1939, the benefit of the platform pitch motion on the power performance of the turbine array is diminished at low TSR^{II}s.

Fig. 23 illustrates the instantaneous flow patterns around the two VAWTs in the *X-Z* plane for different pitch periods T_P^I when VAWT I pitches to the MDP. It can be seen that the wake pattern of VAWT I is more sensitive to the variation of T_P^I than A_P^I. Also, the corresponding wake trajectory changes significantly with the decrease of T_P^I, especially

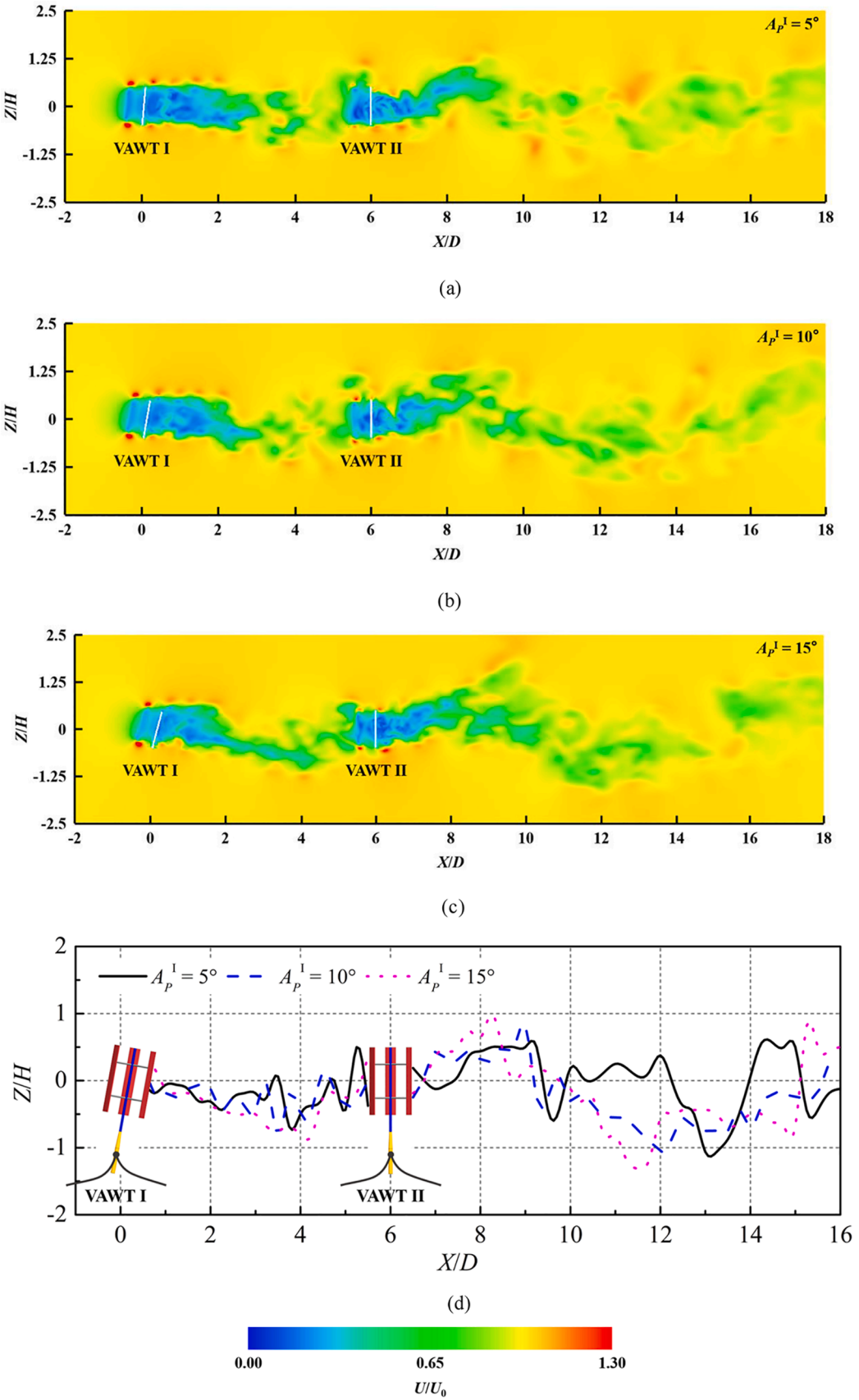

Fig. 20. Instantaneous flow patterns around the two VAWTs in the *X-Z* plane for different pitch amplitudes when VAWT I pitches to the MDP: (a) $A_P^I = 5°$; (b) $A_P^I = 10°$; (c) $A_P^I = 15°$; (d) corresponding wake trajectories, defined by the position where the lowest wake velocity occurs. ($L_S = 6D$, $TSR^I = TSR^{II} = 1.2$, $T_P^I = 4T^I$).

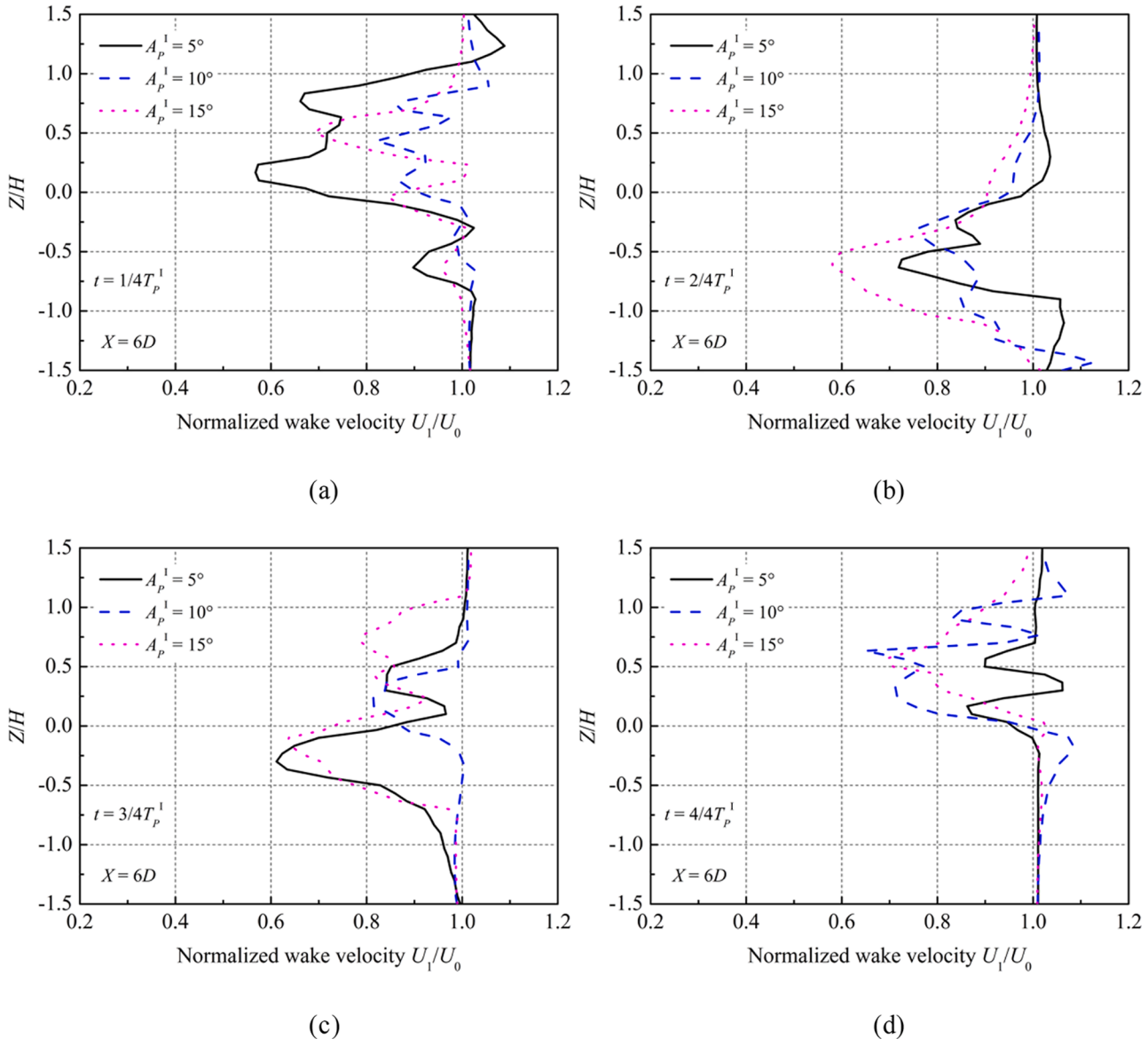

Fig. 21. Normalized instantaneous wake profiles of the pitching VAWT I in the *X-Z* plane at four typical moments for different pitch amplitudes: (a) $t = 1/4T_P^I$; (b) $t = 2/4T_P^I$; (c) $t = 3/4T_P^I$; (d) $t = 4/4T_P^I$. ($X = 6D$, $TSR^I = 1.2$, $T_P^I = 4T^I$).

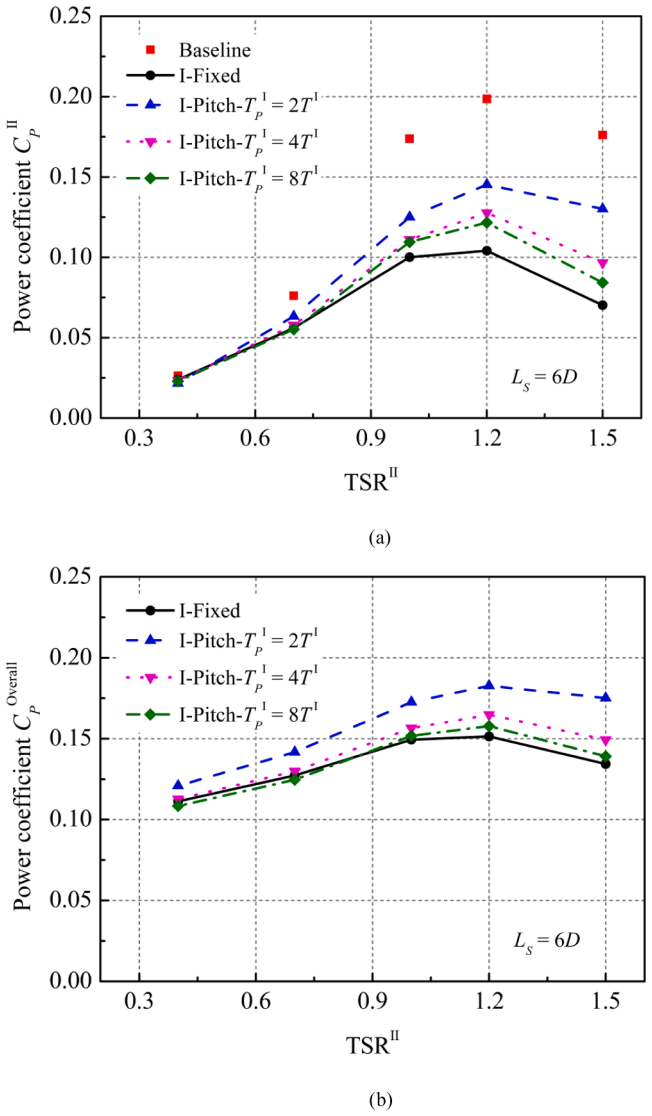

Fig. 22. Averaged power coefficients of the two VAWTs for different pitch periods: (a) C_P^{II}; (b) $C_P^{Overall}$. ($L_S = 6D$, TSR$^I = 1.2$, $A_P^I = 15°$, $C_P^I = 0.2201$, 0.2019, and 0.1939 for $T_P^I = 2T^I$, $4T^I$, and $8T^I$, respectively).

for $T_P^I = 2T^I$: The wake deviation induced by the platform pitch motion is enlarged and the wavelength, i.e., the distance between two consecutive positions where the maximum deviation occurs, is shortened. With these characteristics, more velocity deficit in the core wake region of VAWT I will be spread outward, thereby reducing the wake interference experienced by VAWT II. Besides, as T_P^I decreases, the wake pattern of VAWT II is noticeably disrupted, which is expected to have a considerable impact on the aerodynamics of the VAWTs farther downstream.

Fig. 24 shows the normalized instantaneous wake profiles of the pitching VAWT I in the *X-Z* plane at four typical moments for different pitch periods T_P^I. It can be seen that the configurations of the wake profiles present distinct features for different values of T_P^I. Specifically, on the one hand, the position where the peak of the wake profile occurs is variable, which is because the wavelength of the wake trajectory is sensitive to the variation of T_P^I and thus the deviating direction changes frequently. On the other hand, corresponding to the performance improvement shown in Fig. 22, the velocity deficit in the core wake region is generally reduced as T_P^I decreases, especially for $T_P^I = 2T^I$, which enables VAWT II to experience a higher inflow velocity.

Overall, the relatively larger A_P^I and smaller T_P^I can further alleviate the negative effect of the wake interference on the power performance of VAWT II by changing the wake pattern of VAWT I. However, the vibration and fatigue problems of the pitching VAWTs should also be carefully considered during the design process.

5. Conclusions

In the present study, the high-fidelity IDDES is applied to investigate the wake interference between two tandem offshore floating VAWTs for a scenario, in which the upstream turbine (VAWT I) is under the platform pitch motion and the downstream turbine (VAWT II) is set to bottom-fixed. The effects of different pitch amplitudes and pitch periods on the wake interference are characterized, focusing on the variations of the turbine performance and flow structures. The case in which both VAWTs are set to bottom-fixed is also included for comparison and for exploring the basic layout pattern of the bottom-fixed turbine array. The main conclusions are as follows:

- The power performance of VAWT II is noticeably deteriorated at moderate and high TSR^{II}s due to the large velocity deficit in the wake region of VAWT I. Also, the power performance gradually picks up with the increase of L_S when the optimal TSR^{II} rises correspondingly. In addition, locating VAWT II in the medium wake region of VAWT I, e.g., $L_S = 6D$, can appropriately balance the power performance and space cost of the bottom-fixed turbine array.
- The platform pitch motion of VAWT I can considerably improve the power performance of VAWT II, e.g., the value of C_P^{II} increases by 22.67% when $L_S = 6D$, TSR$^{II} = 1.2$, $A_P^I = 15°$, and $T_P^I = 4T^I$. Larger peak to valley values and more intense fluctuations are observed in the instantaneous C_Q^{II} and C_T^{II}. The corresponding spectral features will not be changed since the $n \times P$ criterion dominates the aerodynamics of the VAWTs.
- The platform pitch motion can make the turbine wake deviate from the centerline and propagate to the downstream region in a wave-like manner. The wake deviation will spread the velocity deficit outside the core wake region of VAWT I, enabling VAWT II to partially avoid the wake interference and experience a higher inflow velocity. The blade-vortex interaction of VAWT II is found to be enhanced and the regular wake development is disrupted.
- The relatively larger pitch amplitudes and smaller pitch periods can further alleviate the negative effect of the wake interference on the power performance of VAWT II by changing the wake pattern of VAWT I, i.e., enlarging the wake deviation and shortening the wavelength to reduce the mean velocity deficit in the core wake region. The relative increments of the peak value of C_P^{II} from $A_P^I = 5°$ to 10° and from $T_P^I = 4T^I$ to $2T^I$ are 19.09% and 13.70%, respectively.
- The platform pitch motion can improve the power performance of the upstream turbine and reduce the wake interference acting on the downstream turbine, thereby enabling the floating VAWT array to achieve a higher power output than the bottom-fixed one. With the potential for higher power density, offshore floating wind farms can be designed more compactly when ensuring a sufficient separation distance required for safety (e.g., avoiding the mooring line interference). However, since the platform pitch motion will expand the influence range of the turbine wake in the vertical direction, some spatial strategies for reducing the wake interference between tandem wind turbines, such as vertically-staggered arrangement, may be limited in practice. In addition, the floating platforms should be carefully designed to obtain reasonable oscillation characteristics so that the wind farms can take advantage of the benefits of the platform pitch motion while controlling the structural vibration and fatigue problems.

6. Present limitations and future perspectives

In the present study, a scaled high-solidity VAWT is selected as the

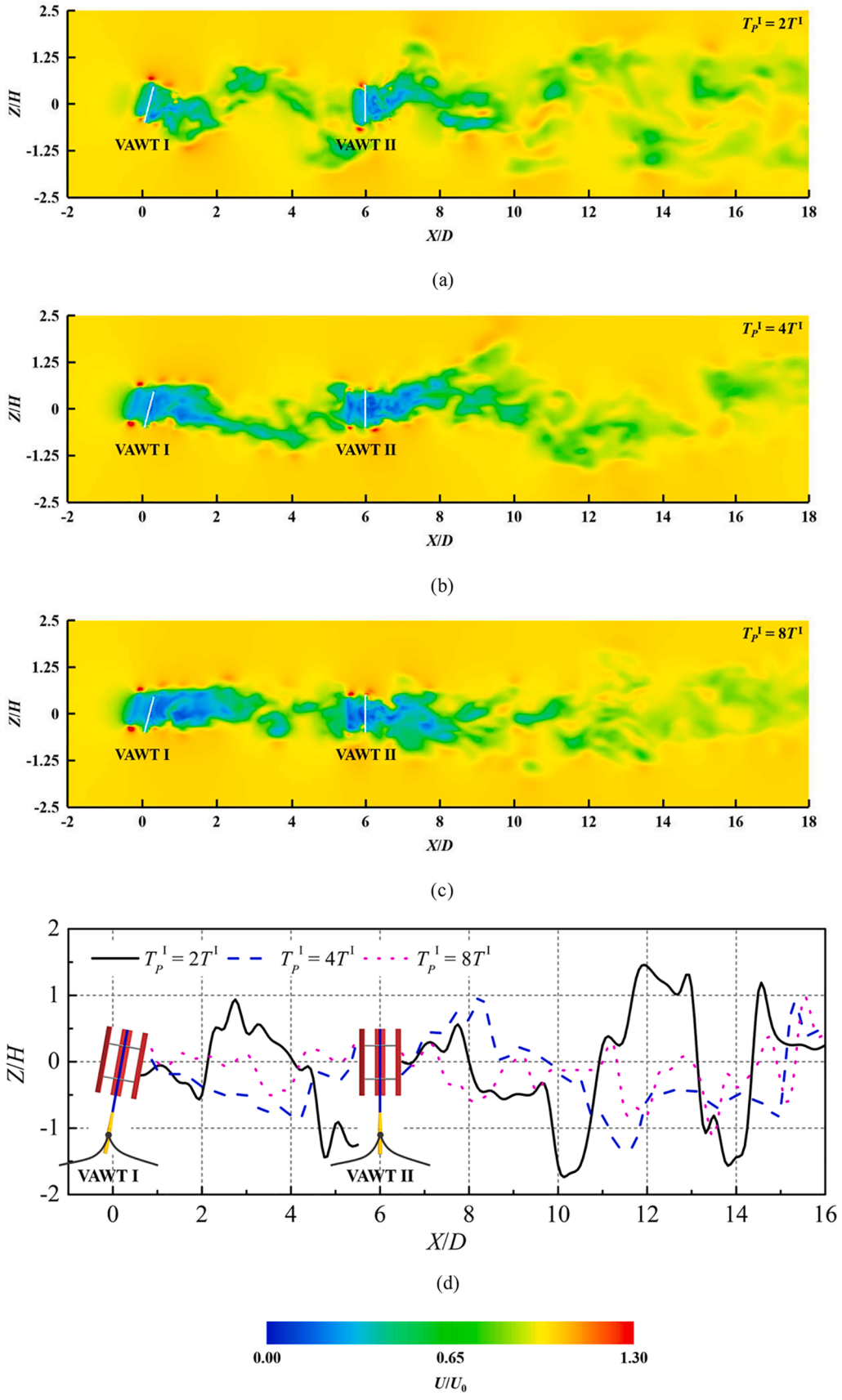

Fig. 23. Instantaneous flow patterns around the two VAWTs in the *X-Z* plane for different pitch periods when VAWT I pitches to the MDP: (a) $T_P^I = 2T^I$; (b) $T_P^I = 4T^I$; (c) $T_P^I = 8T^I$; (d) corresponding wake trajectories. ($L_S = 6D$, $TSR^I = TSR^{II} = 1.2$, $A_P^I = 15°$).

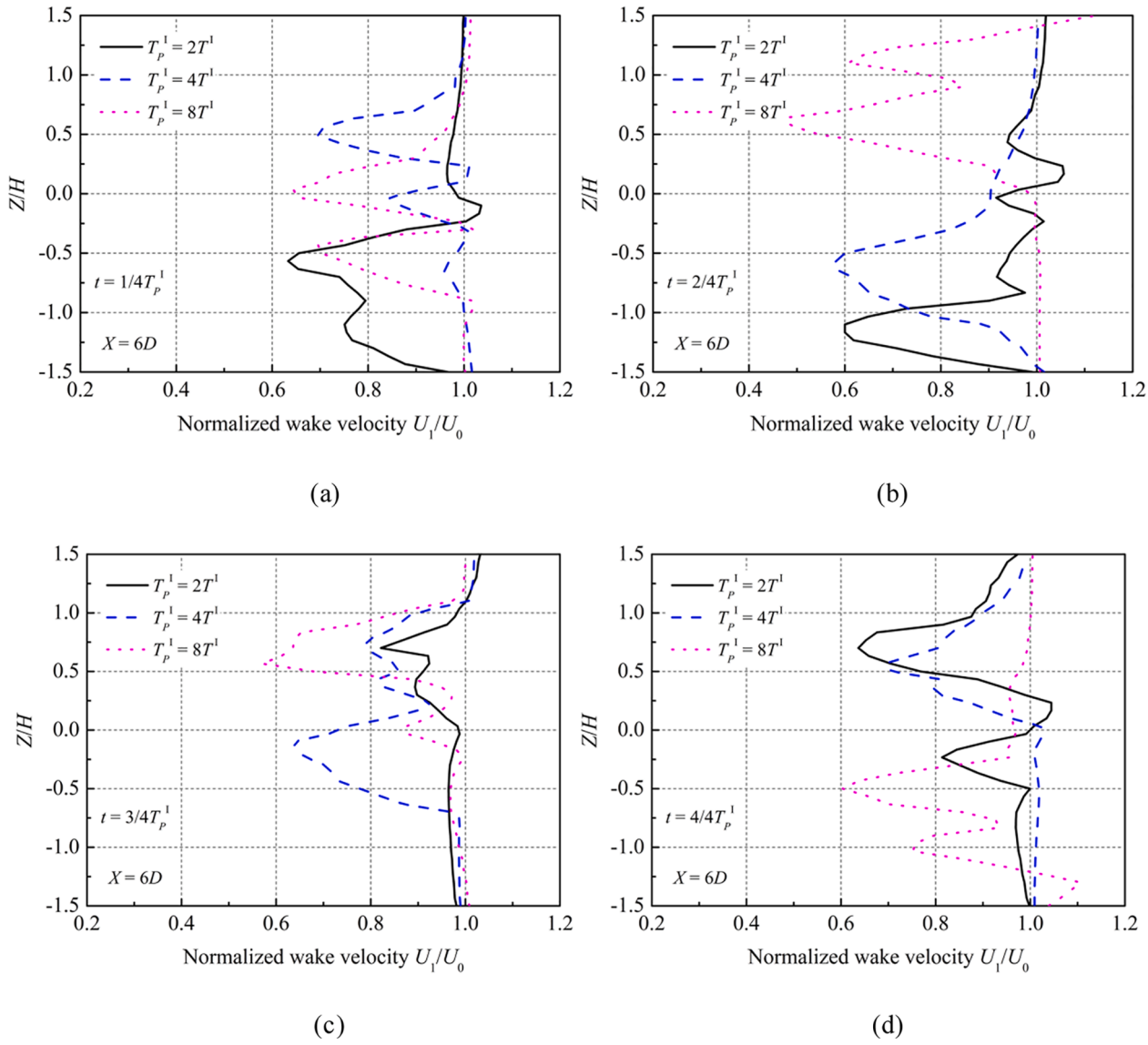

Fig. 24. Normalized instantaneous wake profiles of the pitching VAWT I in the *X-Z* plane at four typical moments for different pitch periods: (a) $t = 1/4T_P^I$; (b) $t = 2/4T_P^I$; (c) $t = 3/4T_P^I$; (d) $t = 4/4T_P^I$. ($X = 6D$, $TSR^I = 1.2$, $A_P^I = 15°$).

upper rotor of the offshore floating wind turbine. On the one hand, the RNSE may lead to an aerodynamic mismatch between the scaled and full-scale turbines [56], thereby affecting the accurate evaluation of the wake interference. On the other hand, the rotor solidity has a considerable impact on the turbine wake and the high-solidity characteristic of the selected VAWT will result in an overestimation of the wake recovery [17], which may affect the generalizability of the study. In the future, the conceptual 5 MW offshore floating VAWT designed by Cheng et al. [63,64] will be employed and the effect of the rotor solidity on the wake interference is expected to be investigated.

The coupled aero-hydrodynamic modeling of the offshore floating VAWTs is another potential improvement for the present study. It enables the turbines to update their positions in real-time according to the wind and wave excitations, instead of being bottom-fixed or floating with a prescribed motion rule. Although the implementation of the multi-physics modeling will increase the computational cost of the simulations, it can improve the realism of the investigative scenarios and provide better insight into the wake interference within the floating turbine array. In addition, the different inflow conditions will be considered and a one-to-one rotation velocity-wind velocity relationship will be applied to determine the TSRs of the wind turbines.

Overall, the present study develops a fundamental understanding of the wake interference between the offshore floating VAWTs. More realistic and complex studies will be conducted in the future, e.g., coupled aero-hydrodynamic analysis of the floating turbine array with multiple full-scale rotors.

CRediT authorship contribution statement

Limin Kuang: Conceptualization, Methodology, Software, Validation, Formal analysis, Writing – original draft, Writing – review & editing. **Qi Lu:** Conceptualization. **Xuan Huang:** Writing – review & editing. **Leijian Song:** Methodology. **Yaoran Chen:** Writing – review & editing. **Jie Su:** Methodology, Software. **Zhaolong Han:** Conceptualization, Resources, Writing – review & editing, Supervision, Funding acquisition. **Dai Zhou:** Resources, Supervision, Funding acquisition. **Yongsheng Zhao:** Funding acquisition. **Yuwang Xu:** Funding acquisition. **Yijie Liu:** Formal analysis.

Declaration of Competing Interest

The authors declare that they have no known competing financial

interests or personal relationships that could have appeared to influence the work reported in this paper.

Acknowledgments

The financial supports from the National Natural Science Foundation of China (Nos. 52122110, 52088102, 42076210, 51909159, and 51879160), Innovation Program of Shanghai Municipal Education Commission (No. 2019-01-07-00-02-E00066), Projects for Intergovernmental Cooperation in International Science, Technology and Innovation (No. 2018YFE0125100), and Oceanic Interdisciplinary Program of Shanghai Jiao Tong University (Nos. SL2021PT302 and SL2020PT201) are gratefully acknowledged.

Appendix A. Supplementary data

Supplementary data to this article can be found online at https://doi.org/10.1016/j.enconman.2022.115769.

References

[1] Ghasemian M, Ashrafi ZN, Sedaghat A. A review on computational fluid dynamic simulation techniques for Darrieus vertical axis wind turbines. Energy Conv Manag 2017;149:87–100.
[2] Roh C, Ha Y, Ahn H, Kim K. A comparative analysis of the characteristics of platform motion of a floating offshore wind turbine based on pitch controllers. Energies 2022;15(3):716.
[3] Hand B, Kelly G, Cashman A. Aerodynamic design and performance parameters of a lift-type vertical axis wind turbine: A comprehensive review. Renew Sust Energ Rev 2021;139:110699.
[4] Ma N, Lei H, Han Z, Zhou D, Bao Y, Zhang K, et al. Airfoil optimization to improve power performance of a high-solidity vertical axis wind turbine at a moderate tip speed ratio. Energy 2018;150:236–52.
[5] Zhao Z, Wang D, Wang T, Shen W, Liu H, Chen M. A review: Approaches for aerodynamic performance improvement of lift-type vertical axis wind turbine. Sustain Energy Technol Assess 2022;49:101789.
[6] Rezaeiha A, Montazeri H, Blocken B. Characterization of aerodynamic performance of vertical axis wind turbines: Impact of operational parameters. Energy Conv Manag 2018;169:45–77.
[7] Kuang L, Su J, Chen Y, Han Z, Zhou D, Zhao Y, et al. Flow characteristics and dynamic responses of a parked straight-bladed vertical axis wind turbine. Energy Sci Eng 2019;7(5):1767–83.
[8] Chen G, Li X, Liang X. IDDES simulation of the performance and wake dynamics of the wind turbines under different turbulent inflow conditions. Energy 2022;238:121772.
[9] Wu Y, Porté-Agel F. Modeling turbine wakes and power losses within a wind farm using LES: An application to the Horns Rev offshore wind farm. Renew Energy 2015;75:945–55.
[10] Nilsson K, Ivanell S, Hansen KS, Mikkelsen R, Sørensen JN, Breton S-P, et al. Large-eddy simulations of the Lillgrund wind farm. Wind Energy 2015;18(3):449–67.
[11] Tescione G, Ragni D, He C, Ferreira CJS, van Bussel GJW. Near wake flow analysis of a vertical axis wind turbine by stereoscopic particle image velocimetry. Renew Energy 2014;70:47–61.
[12] Li Q, Maeda T, Kamada Y, Ogasawara T, Nakai A, Kasuya T. Investigation of power performance and wake on a straight-bladed vertical axis wind turbine with field experiments. Energy 2017;141:1113–23.
[13] Rolin VFC, Porté-Agel F. Experimental investigation of vertical-axis wind-turbine wakes in boundary layer flow. Renew Energy 2018;118:1–13.
[14] Shi W, Jiang J, Sun K, Ju Q. Aerodynamic performance of semi-submersible floating wind turbine under pitch motion. Sustain Energy Technol Assess 2021;48:101556.
[15] Abkar M, Dabiri JO. Self-similarity and flow characteristics of vertical-axis wind turbine wakes: an LES study. J Turbul 2017;18(4):373–89.
[16] Posa A. Influence of Tip Speed Ratio on wake features of a Vertical Axis Wind Turbine. J Wind Eng Ind Aerodyn 2020;197:104076.
[17] Posa A. Dependence of the wake recovery downstream of a Vertical Axis Wind Turbine on its dynamic solidity. J Wind Eng Ind Aerodyn 2020;202:104212.
[18] Shamsoddin S, Porté-Agel F. Effect of aspect ratio on vertical-axis wind turbine wakes. J Fluid Mech 2020;889:R1.
[19] Zuo W, Wang X, Kang S. Numerical simulations on the wake effect of H-type vertical axis wind turbines. Energy 2016;106:691–700.
[20] Kuang L, Lei H, Zhou D, Han Z, Bao Y, Zhao Y. Numerical investigation of effects of turbulence intensity on aerodynamic performance for straight-bladed vertical-axis wind turbines. J Energy Eng-ASCE 2021;147(1):04020087.
[21] Dabiri JO. Potential order-of-magnitude enhancement of wind farm power density via counter-rotating vertical-axis wind turbine arrays. J Renew Sustain Energy 2011;3(4):043104.
[22] Kinzel M, Mulligan Q, Dabiri JO. Energy exchange in an array of vertical-axis wind turbines. J Turbul 2012;13:1–13.
[23] Zanforlin S, Nishino T. Fluid dynamic mechanisms of enhanced power generation by closely spaced vertical axis wind turbines. Renew Energy 2016;99:1213–26.
[24] Sahebzadeh S, Rezaeiha A, Montazeri H. Towards optimal layout design of vertical-axis wind-turbine farms: Double rotor arrangements. Energy Conv Manag 2020;226:113527.
[25] Chen W, Chen C, Huang C, Hwang C. Power output analysis and optimization of two straight-bladed vertical-axis wind turbines. Appl Energy 2017;185:223–32.
[26] Alexander AS, Santhanakrishnan A. Mechanisms of power augmentation in two side-by-side vertical axis wind turbines. Renew Energy 2020;148:600–10.
[27] Peng H, Han Z, Liu H, Lin K, Lam H. Assessment and optimization of the power performance of twin vertical axis wind turbines via numerical simulations. Renew Energy 2020;147:43–54.
[28] Peng HY, Liu MN, Liu HJ, Lin K. Optimization of twin vertical axis wind turbines through large eddy simulations and Taguchi method. Energy 2022;240:122560.
[29] Ahmadi-Baloutaki M, Carriveau R, Ting DSK. A wind tunnel study on the aerodynamic interaction of vertical axis wind turbines in array configurations. Renew Energy 2016;96:904–13.
[30] Lam H, Peng H. Measurements of the wake characteristics of co- and counter-rotating twin H-rotor vertical axis wind turbines. Energy 2017;131:13–26.
[31] Su H, Meng H, Qu T, Lei L. Wind tunnel experiment on the influence of array configuration on the power performance of vertical axis wind turbines. Energy Conv Manag 2021;241:114299.
[32] Borg M, Shires A, Collu M. Offshore floating vertical axis wind turbines, dynamics modelling state of the art. part I: Aerodynamics. Renew Sust Energ Rev 2014;39:1214–25.
[33] Micallef D, Rezaeiha A. Floating offshore wind turbine aerodynamics: Trends and future challenges. Renew Sust Energ Rev 2021;152:111696.
[34] Tran TT, Kim D. The platform pitching motion of floating offshore wind turbine: A preliminary unsteady aerodynamic analysis. J Wind Eng Ind Aerodyn 2015;142:65–81.
[35] Chen G, Liang X, Li X. Modelling of wake dynamics and instabilities of a floating horizontal-axis wind turbine under surge motion. Energy 2022;239:122110.
[36] Lei H, Su J, Bao Y, Chen Y, Han Z, Zhou D. Investigation of wake characteristics for the offshore floating vertical axis wind turbines in pitch and surge motions of platforms. Energy 2019;166:471–89.
[37] Rezaeiha A, Micallef D. Wake interactions of two tandem floating offshore wind turbines: CFD analysis using actuator disc model. Renew Energy 2021;179:859–76.
[38] Rockel S, Peinke J, Hölling M, Cal RB. Wake to wake interaction of floating wind turbine models in free pitch motion: An eddy viscosity and mixing length approach. Renew Energy 2016;85:666–76.
[39] Huang Y, Wan D. Investigation of interference effects between wind turbine and spar-type floating platform under combined wind-wave excitation. Sustainability 2020;12(1):246.
[40] Lei H, Zhou D, Lu J, Chen C, Han Z, Bao Y. The impact of pitch motion of a platform on the aerodynamic performance of a floating vertical axis wind turbine. Energy 2017;119:369–83.
[41] Wen B, Dong X, Tian X, Peng Z, Zhang W, Wei K. The power performance of an offshore floating wind turbine in platform pitching motion. Energy 2018;154:508–21.
[42] Fang Y, Duan L, Han Z, Zhao Y, Yang H. Numerical analysis of aerodynamic performance of a floating offshore wind turbine under pitch motion. Energy 2020;192:116621.
[43] Elkhoury M, Kiwata T, Aoun E. Experimental and numerical investigation of a three-dimensional vertical-axis wind turbine with variable-pitch. J Wind Eng Ind Aerodyn 2015;139:111–23.
[44] Su J, Lei H, Zhou D, Han Z, Bao Y, Zhu H, et al. Aerodynamic noise assessment for a vertical axis wind turbine using Improved Delayed Detached Eddy Simulation. Renew Energy 2019;141:559–69.
[45] Kuang L, Su J, Chen Y, Han Z, Zhou D, Zhang K, et al. Wind-capture-accelerate device for performance improvement of vertical-axis wind turbines: External diffuser system. Energy 2022;239:122196.
[46] CD-adapco. STAR-CCM+ User Guide Version 13.04. CD-adapco: New York, NY, USA 2018.
[47] Shur ML, Spalart PR, Strelets MK, Travin AK. A hybrid RANS-LES approach with delayed-DES and wall-modelled LES capabilities. Int J Heat Fluid Flow 2008;29(6):1638–49.
[48] Lei H, Zhou D, Bao Y, Li Y, Han Z. Three-dimensional Improved Delayed Detached Eddy Simulation of a two-bladed vertical axis wind turbine. Energy Conv Manag 2017;133:235–48.
[49] Ghasemian M, Nejat A. Aerodynamic noise prediction of a Horizontal Axis Wind Turbine using Improved Delayed Detached Eddy Simulation and acoustic analogy. Energy Conv Manag 2015;99:210–20.
[50] Su J, Li Y, Chen Y, Han Z, Zhou D, Zhao Y, et al. Aerodynamic performance assessment of φ-type vertical axis wind turbine under pitch motion. Energy 2021;225:120202.
[51] Wang Z, Zhuang M. Leading-edge serrations for performance improvement on a vertical-axis wind turbine at low tip-speed-ratios. Appl Energy 2017;208:1184–97.
[52] Probst A, Knopp T, Grabe C, Jägersküpper J. HPC requirements of high-fidelity flow simulations for aerodynamic applications. European Conference on Parallel Processing 2019:25.
[53] Rezaeiha A, Kalkman I, Blocken B. CFD simulation of a vertical axis wind turbine operating at a moderate tip speed ratio: Guidelines for minimum domain size and azimuthal increment. Renew Energy 2017;107:373–85.
[54] Dessoky A, Zamre P, Lutz T, Kramer E. Numerical investigations of two Darrieus turbine rotors placed one behind the other with respect to wind direction.

Proceedings of ICFD13: Thirteenth International Conference of Fluid Dynamics 2018:ICFD13-EG-6023.
[55] Swanson WM. The Magnus effect: A summary of investigations to date. J Basic Eng 1961;83(3):461–70.
[56] Wen B, Tian X, Dong X, Li Z, Peng Z, Zhang W, et al. Design approaches of performance-scaled rotor for wave basin model tests of floating wind turbines. Renew Energy 2020;148:573–84.
[57] Wu Y, Liao T, Chen C, Lin C, Chen P. Power output efficiency in large wind farms with different hub heights and configurations. Renew Energy 2019;132:941–99.
[58] Zhang M, Arendshorst MG, Stevens RJAM. Large eddy simulations of the effect of vertical staggering in large wind farms. Wind Energy 2019;22(2):189–204.
[59] Collu M, Borg M, Shires A, Brennan FP. FloVAWT: progress on the development of a coupled model of dynamics for floating offshore vertical axis wind turbines. Proceedings of the ASME 2013 32nd International Conference on Ocean, Offshore and Arctic Engineering 2013:OMAE2013-10717.
[60] Cheng P, Huang Y, Wan D. A numerical model for fully coupled aero-hydrodynamic analysis of floating offshore wind turbine. Ocean Eng 2019;173:183–96.
[61] Rezaeiha A, Montazeri H, Blocken B. Active flow control for power enhancement of vertical axis wind turbines: Leading-edge slot suction. Energy 2019;189:116131.
[62] Tirandaz MR, Rezaeiha A. Effect of airfoil shape on power performance of vertical axis wind turbines in dynamic stall: Symmetric Airfoils. Renew Energy 2021;173:422–41.
[63] Cheng Z, Madsen HA, Gao Z, Moan T. Effect of the number of blades on the dynamics of floating straight-bladed vertical axis wind turbines. Renew Energy 2017;101:1285–98.
[64] Cheng Z, Madsen HA, Chai W, Gao Z, Moan T. A comparison of extreme structural responses and fatigue damage of semi-submersible type floating horizontal and vertical axis wind turbines. Renew Energy 2017;108:207–19.